

## Research Component 1

# Selection of Climate Models for Downscaling

Final version – June 2015

### **Authors**

Arthur Lutz, MSc.  
Dr. Walter Immerzeel  
Dr. Hester Biemans  
Dr. Herbert ter Maat  
Dr. Vidyunmala Veldore  
Dr. Arun Shrestha

**Report FutureWater: 145**

# Table of contents

<b>1</b>	<b>Introduction</b>	<b>6</b>
<b>2</b>	<b>Selection of RCPs</b>	<b>7</b>
<b>3</b>	<b>Spatial and temporal domains</b>	<b>9</b>
3.1	Spatial domain	9
3.2	Statistical downscaled dataset	9
<b>4</b>	<b>Selection of climate models</b>	<b>10</b>
4.1	Advanced envelope based selection approach	10
4.2	Initial selection: Selection on average annual change in means	11
4.3	Refined selection: Selection based on changes in extremes	14
4.4	Final selection: Selection based on GCM validation to climatic reference	19
4.4.1	Skill Assessment of GCMs 1980-2004	20
<b>5</b>	<b>Statistical Downscaling</b>	<b>27</b>
5.1	Historical baseline climate dataset	27
5.1.1	Existing gridded meteorological forcing datasets	27
5.1.2	Station observations	30
5.1.3	New historical baseline climate dataset for the IGB basins	32
5.1.4	Correction of air temperature	33
5.1.5	Correction of precipitation data	35
5.2	Statistical downscaling techniques	40
5.2.1	Perfect Prognosis Statistical Downscaling	41
5.2.2	Model Output Statistics	42
5.2.3	Weather generator approaches	43
5.3	Proposed downscaling approach for future climate	44
	<b>Appendix: Changes in indices for climatic extremes</b>	<b>48</b>
<b>6</b>	<b>References</b>	<b>51</b>



## Tables

Table 1: Description and visualization of the four representative concentration pathways (RCPs).....	7
Table 2: Temporal domain and resolution and spatial resolution and projection for upstream basins. ....	9
Table 3: Temporal domain and resolution and spatial resolution and projection for downstream basins. ....	9
Table 4: Models selected during initial selection based on changes in means. ....	13
Table 5: Indices for climate extremes (ETCCDI indices) used as selection criteria. ....	14
Table 6: Skill scores of the models for both temperature and precipitation for the 6 subbasins based on skill score analysis (LI: Lower Indus, UI: Upper Indus, UB: Upper Brahmaputra, LB: Lower Brahmaputra, LG: Lower Ganges, UG: Upper Ganges). ....	22
Table 7: ranking of the models for the 6 subbasins (LI: Lower Indus, UI: Upper Indus, UB: Upper Brahmaputra, LB: Lower Brahmaputra, LG: Lower Ganges, UG: Upper Ganges). SS P: Skill Score Precipitation, SS T: Skill Score Temperature ....	23
Table 8: The selected models based on the skill score analysis ....	24
Table 9: Overview of gridded meteorological products. ....	28
Table 10: Meteorological ground station records in the upper IGB used in HIAWARE. ....	31
Table 11: Properties of sites in the HKH region where geodetic mass balance data has been analysed by [ <i>Gardelle et al., 2013</i> ].....	36

## Figures

Figure 1: RCPs. blue: RCP8.5, black: RCP6, red: RCP4.5, green: RCP2.6 .....	7
Figure 2: HIAWARE spatial domain. ....	9
Figure 3: Left: CMIP5 grid cells covering the Indus, Ganges and Brahmaputra basins. Right: Illustrative (fictive) example showing ensemble of GCMs with projected average changes in temperature and precipitation and ensemble's 10 <sup>th</sup> and 90 <sup>th</sup> percentile values. ....	10
Figure 4: Projections of temperature and precipitation change for all CMIP5 ensemble members in RCP4.5 and RCP8.5. Projections are averaged over the HIAWARE domain (Figure 3). ....	11
Figure 5: Projected changes in temperature and precipitation for RCP4.5 ensemble members. Models selected during the initial selection are highlighted. ....	12
Figure 6: Projected changes in temperature and precipitation for RCP8.5 ensemble members. Models selected during the initial selection are highlighted. ....	13
Figure 7: Changes in precipitation sum and changes in precipitation extremes indicators for CMIP5 RCP4.5 models. ....	15
Figure 8: Changes in precipitation sum and changes in precipitation extremes indicators for CMIP5 RCP8.5 models. ....	16
Figure 9: Changes in mean temperature and changes in temperature extremes indicators for CMIP5 RCP4.5 models .....	16
Figure 10: Changes in mean temperature and changes in temperature extremes indicators for CMIP5 RCP8.5 models .....	17
Figure 11: Projected changes in climatic extremes indicators and mean temperature and precipitation for RCP4.5 model runs selected in section 4.2. Model runs selected for checking to a climatic reference dataset are highlighted orange. ....	18



Figure 12: Projected changes in climatic extremes indicators and mean temperature and precipitation for RCP8.5 model runs selected in section 4.2. Model runs selected for checking to a climatic reference dataset are highlighted orange. ....	19
Figure 13: Outline of the subbasins used in reality checking climate information; purple: lower Indus, dark blue: upper Indus, yellow: lower Ganges, orange: upper Ganges, light blue: upper Brahmaputra, green: lower Brahmaputra. ....	20
Figure 14: Average annual cycles of temperature (C) per GCM and per subbasin (red: selected GCMs, light red: not selected GCMs) and WFDEI (blue). ....	25
Figure 15: Average annual cycles of precipitation (mm) per GCM and per subbasin (red: selected GCMs, light red: not selected GCMs) and WFDEI (blue). ....	26
Figure 16: High-resolution historical climate data is combined with low resolution GCM data to generate high resolution future climate data. ....	27
Figure 17: Multiannual mean (1998-2007) of summer (JJAS) precipitation over the HKKH region as represented by different dataset [ <i>Palazzi et al., 2013</i> ]. ....	29
Figure 18: Multiannual mean (1998-2007) of winter (DJFMA) precipitation over the HKH region as represented by different dataset [ <i>Palazzi et al., 2013</i> ]. ....	30
Figure 19: Locations of meteorological stations in the upper IGB basins. ....	30
Figure 20: Conceptual model of vertical and horizontal meteorological and cryospheric regimes in the Karakoram [ <i>Hewitt, 2007b</i> ]. ....	32
Figure 21: Average temperature lapse rates in 1999 in the upper IGB basins daily calculated from the ERA-INTERIM grid cells and their elevations, covering the upper IGB. ....	33
Figure 22: Bias between observed temperatures and gridded temperatures per month (in °C, y-axis). The x-axis shows the station's elevations. Red dots represent the average bias for 29 individual stations. The blues line shows the linear regression through the red dots, the blue dots show the average bias of the 29 stations. ....	34
Figure 23: Sites in the HKH region where geodetic mass balance data has been analysed by [ <i>Gardelle et al., 2013</i> ]. ....	36
Figure 24: Average glacier mass balance ( $m \text{ we yr}^{-1}$ ) for glaciers within the geodetic mass balance analysis sites [ <i>Gardelle et al., 2013</i> ] in the upper IGB basins. Dots are scaled to glacier surface area. ....	37
Figure 25: Same as Figure 24, but for the Hindu Kush site. ....	37
Figure 26: Same as Figure 24, but for the Karakoram (upper panel), Spiti Lahaul (middle panel), and West-Nepal (lower panel) sites. ....	38
Figure 27: Same as Figure 22, but for the Everest (upper panel), Bhutan (middle panel), and Hengduan Shan (lower panel) sites. ....	39
Figure 28: Scheme of different downscaling approaches (adapted from [ <i>Thiemeßl et al., 2011a</i> ]). ....	40
Figure 29: Seasonal and annual errors uncorrected RCM and the seven DECMs in sub-region 6 (western Austria, high Alpine, upper panels), sub-region 8 (southeast Austra, lower Alpine, middle panels) and for entire Austria (lower panels). The boxes show the 75th percentile (upper limit), the median (line within the box) and the 25th (lower limit). The respective mean observed precipitation amount is given in the header of each panel. The statistics result from station-wise evaluation of daily precipitation data and are spatially averaged [ <i>Thiemeßl et al., 2011a</i> ]. ....	43
Figure 30: Illustrative example of GCM signal downscaling by Quantile Mapping for one grid cell. Upper panel: All daily observations and GCM control run values for days in July during control period (1981-2010). Middle panel: Empirical distribution functions (ecdf) constructed for observations and GCM control run values in upper panel. Lower panel: Future daily temperature for a July in the future as from raw GCM input and corresponding downscaled values. ....	45
Figure 31: Illustrative example of GCM signal downscaling by Quantile Mapping for one grid cell. Upper panel: All daily observations and GCM control run values for days in July during control	



period (1981-2010). Middle panel: Empirical distribution functions (ecdf) constructed for observations and GCM control run values in upper panel. Lower panel: Future daily temperature for a July in the future as from raw GCM input and corresponding downscaled values. .... 47

Figure 32: Projected changes in climate indices between 1971-2000 and 2071-2100 for RCP4.5 multi-model ensemble. .... 49

Figure 33: Projected changes in climate indices between 1971-2000 and 2071-2100 for RCP8.5 multi-model ensemble. .... 50



# 1 Introduction

In HI-AWARE both statistical and dynamical downscaling techniques will be used. For both approaches GCMs/RCMs are required to be selected to be either statistically downscaled or to be used as boundary and forcing for the dynamical downscaling. This report discusses the statistical downscaling component. There are two fundamentally different methods to select appropriate GCMs/RCMs. The first approach aims at covering the full envelope of possible futures ranging from dry and cold projections to wet and warm projections, while the second approach selects GCMs/RCMs on the basis of indicators of past performance. Both approaches have their pros and cons, but in the case of the HKH the first approach may be preferable as climate models have considerable difficulty in simulating past climate [Turner and Annamalai, 2012]. In this study, we develop a new method that combines the two existing methods. We aim to select a set of climate models that both cover a wide range of possible futures, but are also able to reproduce the most important processes in the region.

An extension of the first approach is used and the selected models will span the entire range of possible futures, e.g. dry-cold, dry-warm, wet-cold and wet-warm. In total 4 GCMs and 1 CORDEX RCM for both RCPs will be selected, e.g.  $5 \times 2 = 10$  climate model realizations. Selections are based on average annual response, changes in extreme behaviour in temperature of precipitation and validation of model performance to a climatic reference dataset. These models will be used during the whole project.



## 2 Selection of RCPs

In the climate modelling community, four representative concentration pathways (RCPs) are used as a basis for long-term and near-term climate modeling experiments [Vuuren van et al., 2011]. The four RCPs together span the range of radiative forcing values for the year 2100 as found in literature, from 2.6 to 8.5 W/m<sup>2</sup> (Table 1, Figure 1). Climate modelers use the time series of future radiative forcing from the four RCPs for their climate modeling experiments and produce climate scenarios. The development of the RCPs allowed climate modelers to proceed with experiments in parallel to the development of emission and socio-economic scenarios [Moss et al., 2010]. The four selected RCPs were considered to be representative of the literature, and included one mitigation scenario (RCP2.6), two medium stabilization scenarios (RCP4.5/RCP6) and one very high baseline emission scenario (RCP8.5) [Vuuren van et al., 2011].

**Table 1: Description and visualization of the four representative concentration pathways (RCPs).**

RCP	Description
<b>RCP8.5</b>	Rising radiative forcing pathway leading to 8.5 W/m <sup>2</sup> (~1370 ppm CO <sub>2</sub> eq) by 2100
<b>RCP6</b>	Stabilization without overshoot pathway to 6 W/m <sup>2</sup> (~850 ppm CO <sub>2</sub> eq) at stabilization after 2100
<b>RCP4.5</b>	Stabilization without overshoot pathway to 4.5 W/m <sup>2</sup> (~650 ppm CO <sub>2</sub> eq) at stabilization after 2100
<b>RCP2.6</b>	Peak in radiative forcing at ~3 W/m <sup>2</sup> (~490 ppm CO <sub>2</sub> eq) before 2100 and then decline (the selected pathway declines to 2.6 W/m <sup>2</sup> by 2100)

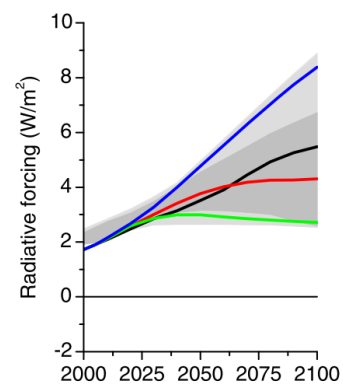


**Figure 1: RCPs. blue: RCP8.5, black: RCP6, red: RCP4.5, green: RCP2.6**

Since the four RCPs are considered to be representative of radiative forcing that can be expected by 2100 according to the literature, each of them should theoretically be considered with equal probability to be included in climate change impact studies. However, in climate change impact studies there is usually a tradeoff in how many RCPs and how many climate models can be included within the available time and resources, whilst at the same time having the necessity of producing robust and reliable results.

RCP2.6 is representative of the literature on mitigation scenarios aiming to limit the increase of global mean temperature to 2 °C, thus forming the low end of the scenario literature in terms of emissions and radiative forcing [van Vuuren et al., 2011]. Often these scenarios show negative emissions from energy use in the second half of the 21<sup>st</sup> century. The scenario is shown to be technically feasible, but one of the key assumptions is the full participation of all countries in the world in the short run, including broadening participation beyond OECD countries, and commitment of important OECD countries like the USA. [van Vuuren et al., 2010]. However, outcomes of recent climate summits at the highest level and the annual Conferences of Parties resulting from the United Nations Framework Convention on Climate Change don't point in that direction. In HI-AWARE, robust, realistic climate change scenarios need to be developed to facilitate the planning of adaptation measure. Therefore we choose not to include RCP2.6 as one of the RCPs used as basis for the HI-AWARE climate model ensemble. This leaves the

choice to two medium stabilization scenarios (RCP4.5 and RCP6) and one very high baseline emission scenario (RCP8.5). The best choice in that case is to include RCP4.5 and RCP8.5, thus including one medium stabilization scenario and the high emission scenario, and covering the entire range of radiative forcing resulting from RCP4.6, RCP6 and RCP8.5. The climate model archives (CMIP5<sup>1</sup> and CORDEX<sup>2</sup>) are used to select a number of GCMs and RCMs for these two different representative concentration pathways.

---

<sup>1</sup> <http://pcmdi9.llnl.gov/esgf-web-fe/>

<sup>2</sup> <http://cordex.dmi.dk/joomla/>



# 3 Spatial and temporal domains

## 3.1 Spatial domain

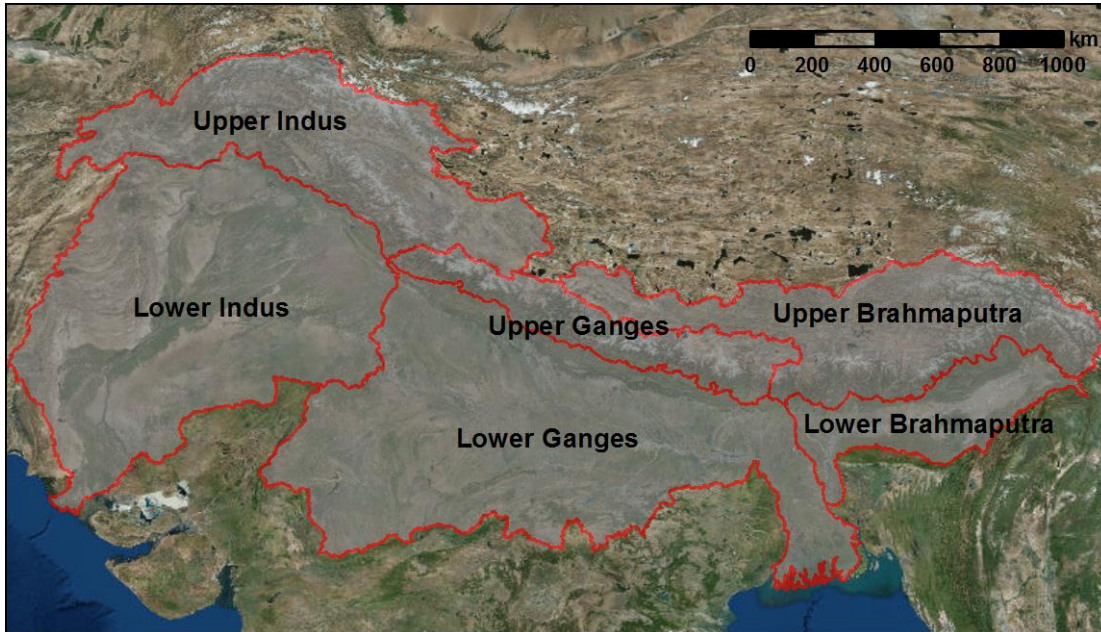


Figure 2: HIWARE spatial domain.

## 3.2 Statistical downscaled dataset

The spatial resolutions in the tables below are tentative and open for discussion. As temporal domain we proposed to have a transient time series. Alternatively, two future time slices (both spanning 30 years) could be defined. The periods could for example be near future (2031-2060) and far future (2071-2100). The decision for transient time series or time slices will have practical implications for the model runs. Transient runs are easier to do, but require a longer series of data, thus more computation time and storage space. Besides, there is a tradeoff in the length of the time series and the spatial resolution that can be adopted.

Table 2: Temporal domain and resolution and spatial resolution and projection for upstream basins.

	Period	Temporal resolution	Spatial resolution	Projection
Historical Baseline	1981-2010	Daily	5 x 5 km	WGS 84 / UTM zone 45N
Future	2011-2100	Daily	5 x 5 km	WGS 84 / UTM zone 45N

Table 3: Temporal domain and resolution and spatial resolution and projection for downstream basins.

	Period	Temporal resolution	Spatial resolution	Projection
Historical Baseline	1981-2010	Daily	10 x 10 km	WGS 84 / UTM zone 45N
Future	2011-2100	Daily	10 x 10 km	WGS 84 / UTM zone 45N

## 4 Selection of climate models

### 4.1 Advanced envelope based selection approach

For each RCP, multiple modeling experiment outcomes are available. The outcomes of the General Circulation Models (GCMs) that were used for the IPCC's fifth assessment report (AR5), are bundled in the fifth phase of the Climate Model Intercomparison Project (CMIP5, [Taylor et al., 2012]). The envelope approach for selecting climate models considers each models' projected average change of a climatic variable over the grid cells that cover a study domain (Figure 3). When considering multiple climatic variables, like mean air temperature and annual precipitation sum, an envelope can be drawn around all possible projections for mean air temperature and precipitation change. From the model ensemble, the 10<sup>th</sup> and 90<sup>th</sup> percentile values of the temperature projections and the 10<sup>th</sup> and 90<sup>th</sup> percentile values of the precipitation projections can be marked, and the climate models closest to these values are selected to be included in the model ensemble that is used for the climate change impact study (see also the illustrative example in Figure 3). This ensures that the entire range of possible future climates in terms of temperature and precipitation change is included, whilst the furthest outliers, which might be unrealistic, are excluded. For the selection of GCMs for downscaling, a three steps selection procedure is used:

1. Initial selection based on average annual changes in the mean temperature and precipitation sum
2. Refined selection based on changes in extremes of precipitation and temperature
3. Final selection based on validation of GCM performance to climatic reference product

Steps 2 and 3 go beyond the envelope method as it is usually used, and adds a past performance check to ensure the best possible selection.

The three steps are further illustrated in the following sections.

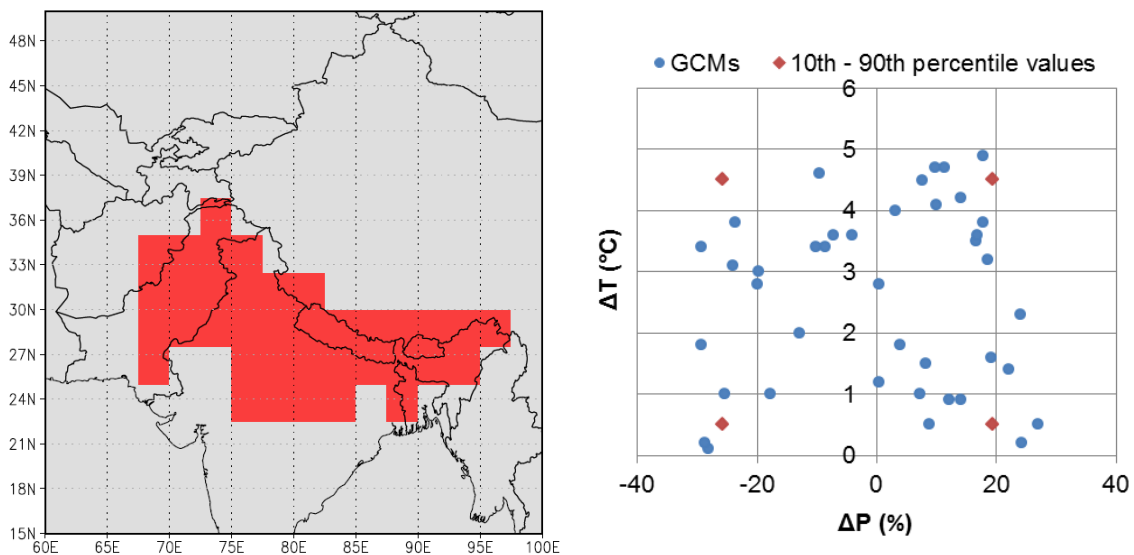


**Figure 3: Left: CMIP5 grid cells covering the Indus, Ganges and Brahmaputra basins. Right: Illustrative (fictive) example showing ensemble of GCMs with projected average changes in temperature and precipitation and ensemble's 10<sup>th</sup> and 90<sup>th</sup> percentile values.**



## 4.2 Initial selection: Selection on average annual change in means

Figure 3 (left) shows the grid cells included in the HIAWARE domain for which the GCM projections are analysed. This domain covers the entire Indus, Ganges and Brahmaputra river basins. Figure 4 shows the projected changes in temperature and precipitation averaged over the HIAWARE domain between 1971-2000 and 2071-2100. RCP4.5 has 94 ensemble members, whereas RCP8.5 has 69 ensemble members. These are all model runs that were available in the CMIP5 archive on March 2013, and represent the state of the archive that was used for the preparation of IPCC Working Group 1 Assessment Report 5 Annex I "Atlas". The figure shows that for RCP4.5 the temperature projections range from +1.7 to +3.6 °C and precipitation projections range from -5.7 to +9.4%. For RCP8.5 the temperature projections range from +3.6 to +6.5 °C and precipitation projections range from -8.5% to +37.4%.

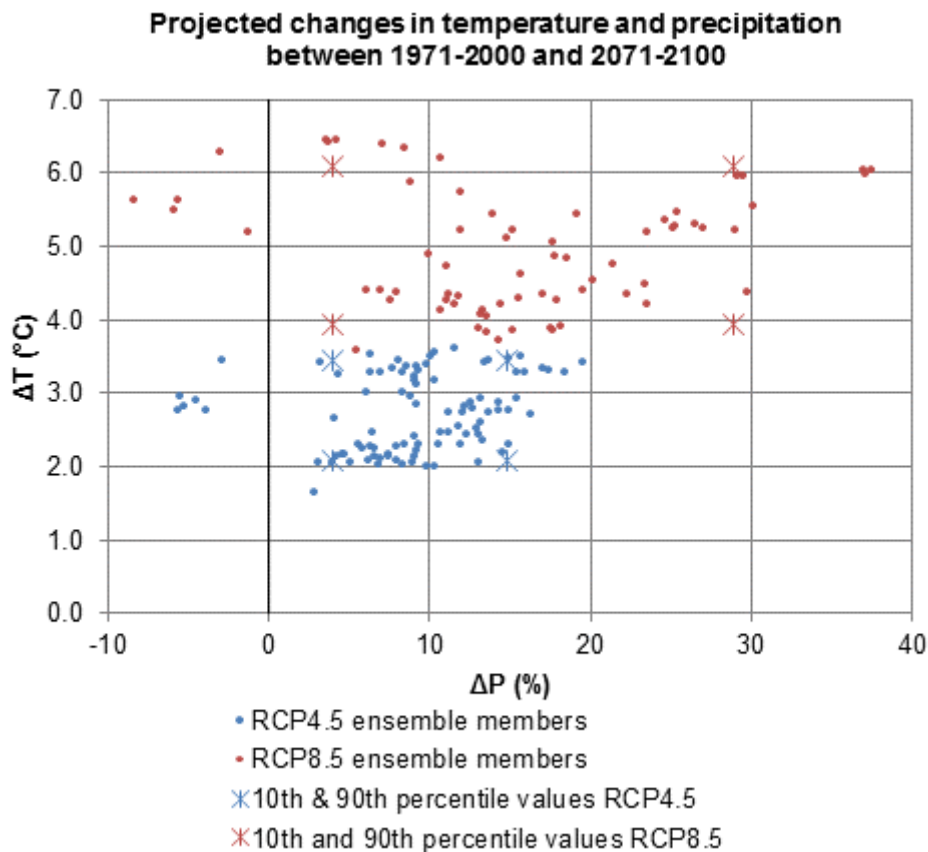


**Figure 4: Projections of temperature and precipitation change for all CMIP5 ensemble members in RCP4.5 and RCP8.5. Projections are averaged over the HIAWARE domain (Figure 3).**

An initial selection of climate models is made by selecting the five models clustered closest to the 10<sup>th</sup> and 90<sup>th</sup> percentile vertices of  $\Delta T$  and  $\Delta P$ , which have output available at a daily time step. A part of the model runs have only output available at a monthly time step. However, these are not suitable for further use in HI-AWARE, since the downscaling procedure that is used after model selection requires GCM output at a daily time step. The proximity of the GCMs to the vertices is calculated based on their percentile rank scores corresponding to their projections for  $\Delta T$  and  $\Delta P$  considering the entire range of projections in the complete ensemble:

$$D_{P_i^T, P_i^P} = \sqrt{((P_i^T - P_j^T)^2 + (P_i^P - P_j^P)^2)}$$

Where  $D_{P_i^T, P_i^P}$  is the distance of a model's (j) percentile score for  $\Delta T$  and  $\Delta P$  ( $P_j^T$  and  $P_j^P$  respectively) to the corner's (i) 10<sup>th</sup> and/or 90<sup>th</sup> percentile score of  $\Delta T$  and  $\Delta P$  for the entire ensemble ( $P_i^T$  and  $P_i^P$  respectively). For each corner the five models with the lowest D and data available at daily time step are selected from the ensemble.

In total around 5 models x 4 vertices x 2 RCPs = 40 models are selected. Figure 5 and Figure 6 show the model ensembles of RCP4.5 and RCP8.5 respectively, including highlighting of the models close to the vertices that have output at a daily time step available, which are selected during the initial selection. Five models close to the 10<sup>th</sup> and 90<sup>th</sup> percentile vertices (cold/dry, cold/wet, warm/dry, warm/wet) of the temperature and precipitation projections are selected. The selected model runs are listed in Table 4, including their projected change in mean temperature and precipitation, averaged over the IGB basins, between 1971-2000 and 2071-2100.

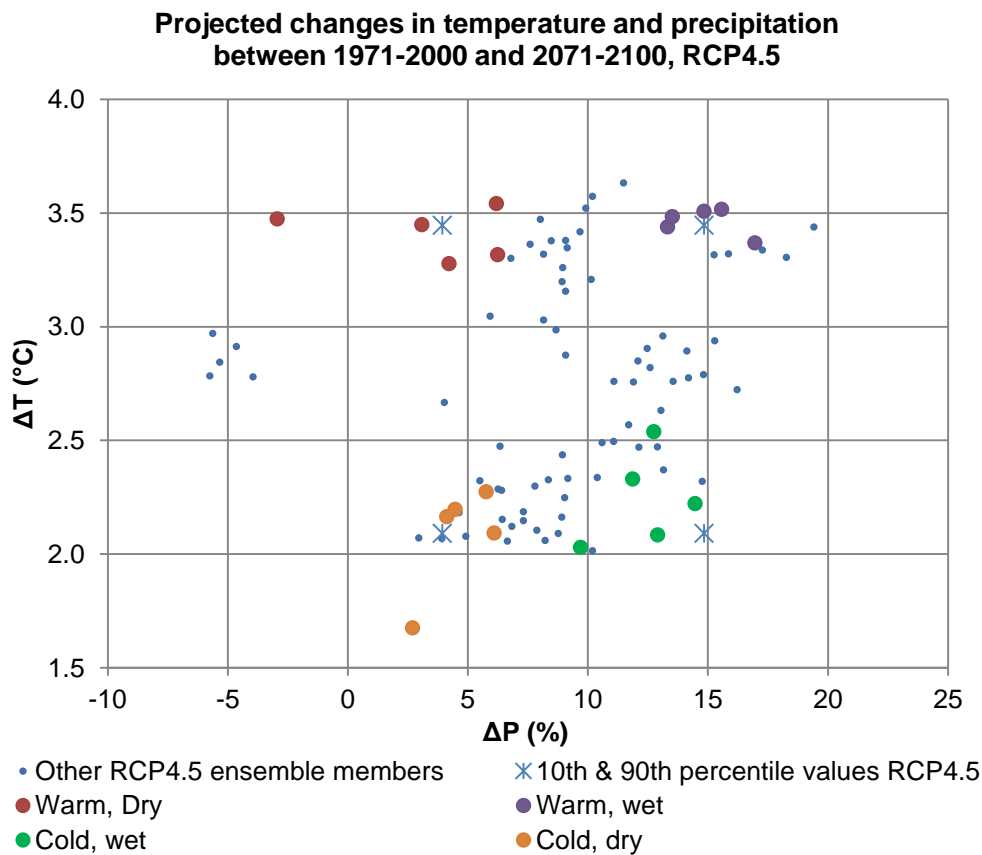


**Figure 5: Projected changes in temperature and precipitation for RCP4.5 ensemble members. Models selected during the initial selection are highlighted.**



Projected changes in temperature and precipitation  
between 1971-2000 and 2071-2100, RCP8.5

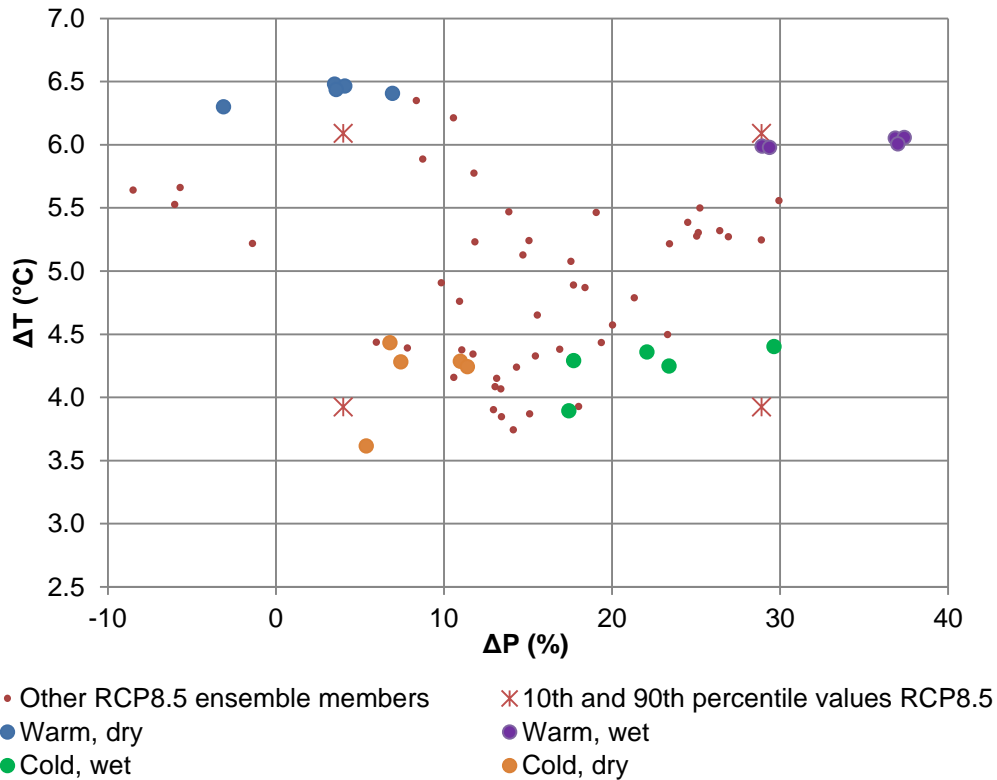


Figure 6: Projected changes in temperature and precipitation for RCP8.5 ensemble members. Models selected during the initial selection are highlighted.

Table 4: Models selected during initial selection based on changes in means.

RCP	Vertex	Model	$\Delta T$	$\Delta P$
RCP4.5	Warm, dry	CMCC-CM_r1i1p1	3.3	4.2
		CMCC-CMS_r1i1p1	3.5	-2.9
		IPSL-CM5A-LR_r2i1p1	3.4	3.1
		IPSL-CM5A-LR_r3i1p1	3.3	6.2
		IPSL-CM5A-MR_r1i1p1	3.5	6.2
	Warm, wet	CanESM2_r1i1p1	3.4	17.0
		CSIRO-Mk3-6-0_r3i1p1	3.4	13.3
		CSIRO-Mk3-6-0_r4i1p1	3.5	15.6
		CSIRO-Mk3-6-0_r5i1p1	3.5	14.8
		CSIRO-Mk3-6-0_r6i1p1	3.5	13.5
	Cold, wet	bcc-csm1-1_r1i1p1	2.2	14.5
		BNU-ESM_r1i1p1	2.5	12.7
		CCSM4_r2i1p1	2.0	9.7
		CNRM-CM5_r1i1p1	2.3	11.9
		IPSL-CM5B-LR_r1i1p1	2.1	12.9
	Cold, dry	bcc-csm1-1-m_r1i1p1	2.3	5.8
		CCSM4_r6i1p1	2.2	4.5
		CESM1-BGC_r1i1p1	2.1	6.1
		GISS-E2-R_r6i1p1	2.2	4.1
		inmcm4_r1i1p1	1.7	2.7



		RCP8.5	
		ETCCDI index	Description
Warm, dry	CMCC-CMS_r1i1p1	6.3	-3.1
	IPSL-CM5A-LR_r1i1p1	6.5	3.5
	IPSL-CM5A-LR_r2i1p1	6.5	4.1
	IPSL-CM5A-LR_r3i1p1	6.4	6.9
	IPSL-CM5A-LR_r4i1p1	6.4	3.6
Warm, wet	CanESM2_r1i1p1	6.0	28.9
	CanESM2_r2i1p1	6.1	36.9
	CanESM2_r3i1p1	6.1	37.4
	CanESM2_r4i1p1	6.0	29.4
	CanESM2_r5i1p1	6.0	37.0
Cold, wet	bcc-csm1-1_r1i1p1	4.4	29.7
	CNRM-CM5_r1i1p1	3.9	17.4
	IPSL-CM5B-LR_r1i1p1	4.2	23.4
	MIROC5_r1i1p1	4.3	17.7
	MRI-CGCM3_r1i1p1	4.4	22.1
Cold, dry	CCSM4_r1i1p1	4.3	11.0
	CCSM4_r6i1p1	4.2	11.4
	EC-EARTH_r2i1p1	4.4	6.8
	EC-EARTH_r9i1p1	4.3	7.4
	inmcm4_r1i1p1	3.6	5.4

### 4.3 Refined selection: Selection based on changes in extremes

From the pool of models selected during the initial selection, a refined selection is made. The refined selection is based on changes in other climate indices indicating changes in climatic extremes. For the refinement of the selection we are most interested in extremes in temperature and precipitation. [Sillmann *et al.*, 2013a] developed a database with analysis of extreme climate indices of CMIP5 GCM runs. They also evaluated the ability of CMIP5 models to simulate climate extremes in the present climate. The researchers concluded that the CMIP5 models are generally able to simulate climate extremes and their trend patterns at the global scale. They show that the representation of precipitation extremes is closer to reality in the CMIP5 ensemble compared to the CMIP3 ensemble. However, the authors expect that the climate models tend to under-simulate the magnitude of precipitation extremes as represented in the climatic reference dataset they used. To quantify the changes in extremes in CMIP5 models, we include two climatic indicators for changes in precipitation extremes and two indicators for changes in temperature extremes in our analysis (Table 5).

**Table 5: Indices for climate extremes (ETCCDI indices) used as selection criteria.**

Variable	ETCCDI index	Description
P	R99pTOT	precipitation due to extremely wet days (> 99 <sup>th</sup> percentile)
P	CDD	consecutive dry days: maximum length of dry spell ( $P < 1$ mm)
T	WSDI	warm spell duration index: count of days in a span of at least six days where $TX > 90^{\text{th}}$ percentile ( $TX_{ij}$ is the daily Tmax on day $i$ in period $j$ )
T	CSDI	Cold spell duration index: count of days in a span of at least six days where $TN > 10^{\text{th}}$ percentile ( $TN_{ij}$ is the daily Tmin on day $i$ in period $j$ )



For precipitation we include an index for extreme high precipitation (precipitation due to extremely wet days), and an index for droughts (maximum length of dry spells). For temperature we include an index for warm extreme events (warm spell duration index), and an index for cold extreme events (cold spell duration index).

Based on this selection, around 2 models per vertex will remain, thus in total around 2 models x 4 vertices x 2 RCPs = 16 models. As not all GCM runs which are available for the analysis of changes in means have been included in the database of [Sillmann *et al.*, 2013a, 2013b], the indices were calculated separately for those models using the R package that was developed to generate the database of CMIP5 extremes and following the same procedure as described in [Sillmann *et al.*, 2013a].

The changes in mean precipitation are for most models closely related to the changes precipitation sum (Figure 7 and Figure 8). It is clear that in general the models with larger projected increases in total precipitation also project larger increase in R99pTOT and larger decrease in CDD. However, the correlation is certainly not 1:1. For both RCPs for example the wettest model is also the model with largest increase in precipitation due to very high precipitation events, but does not have the strongest decrease in consecutive dry days. Similarly, the model with the lowest increase in precipitation due to extremely wet days is not the driest model.

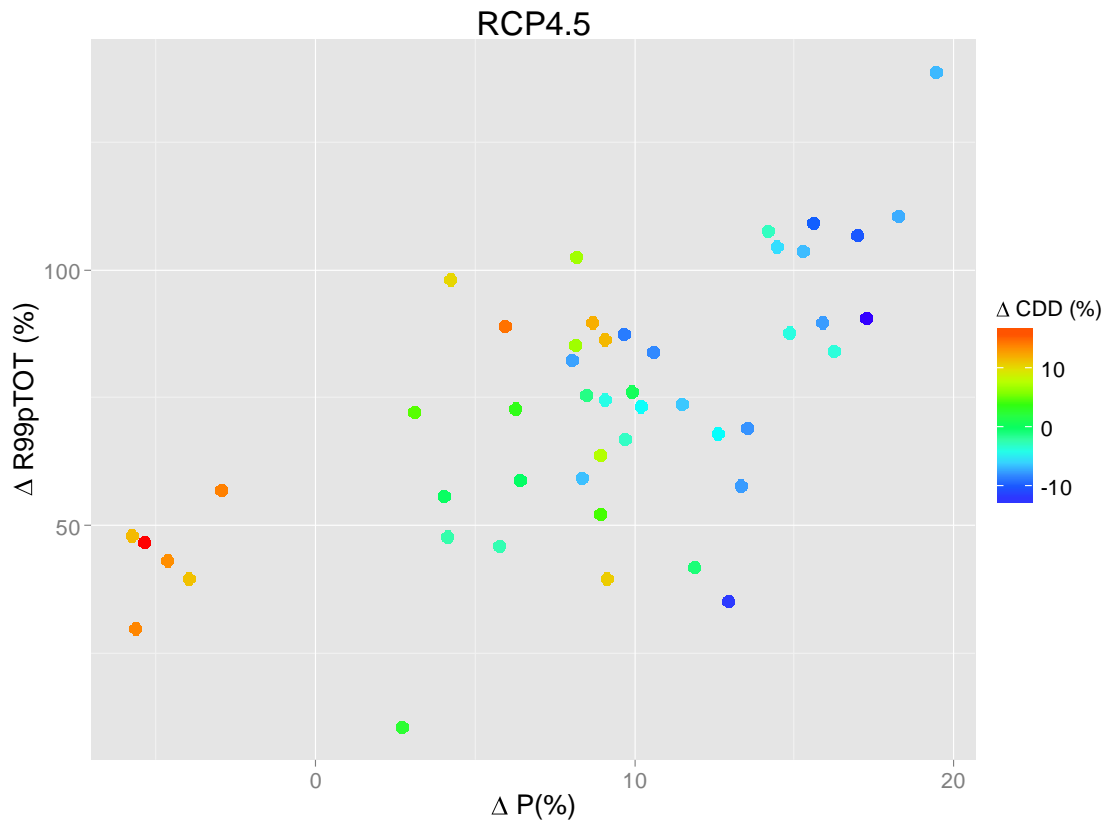


**Figure 7: Changes in precipitation sum and changes in precipitation extremes indicators for CMIP5 RCP4.5 models.**



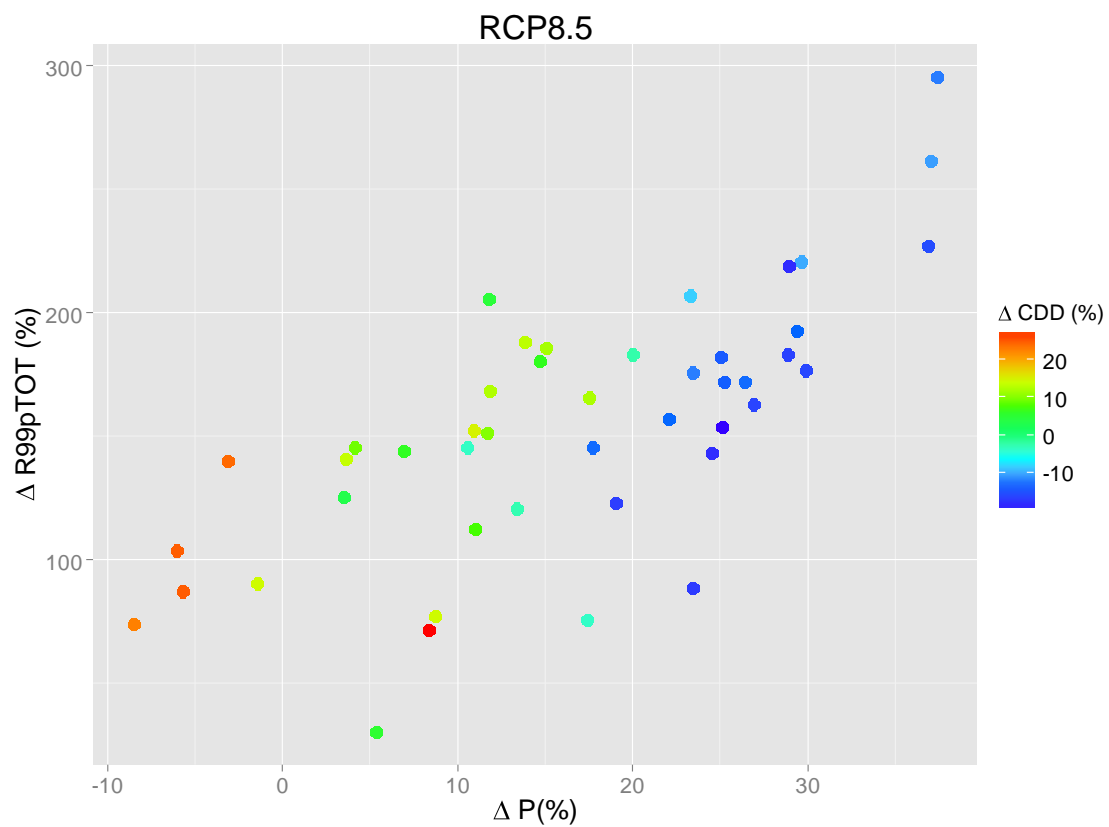


**Figure 8: Changes in precipitation sum and changes in precipitation extremes indicators for CMIP5 RCP8.5 models.**

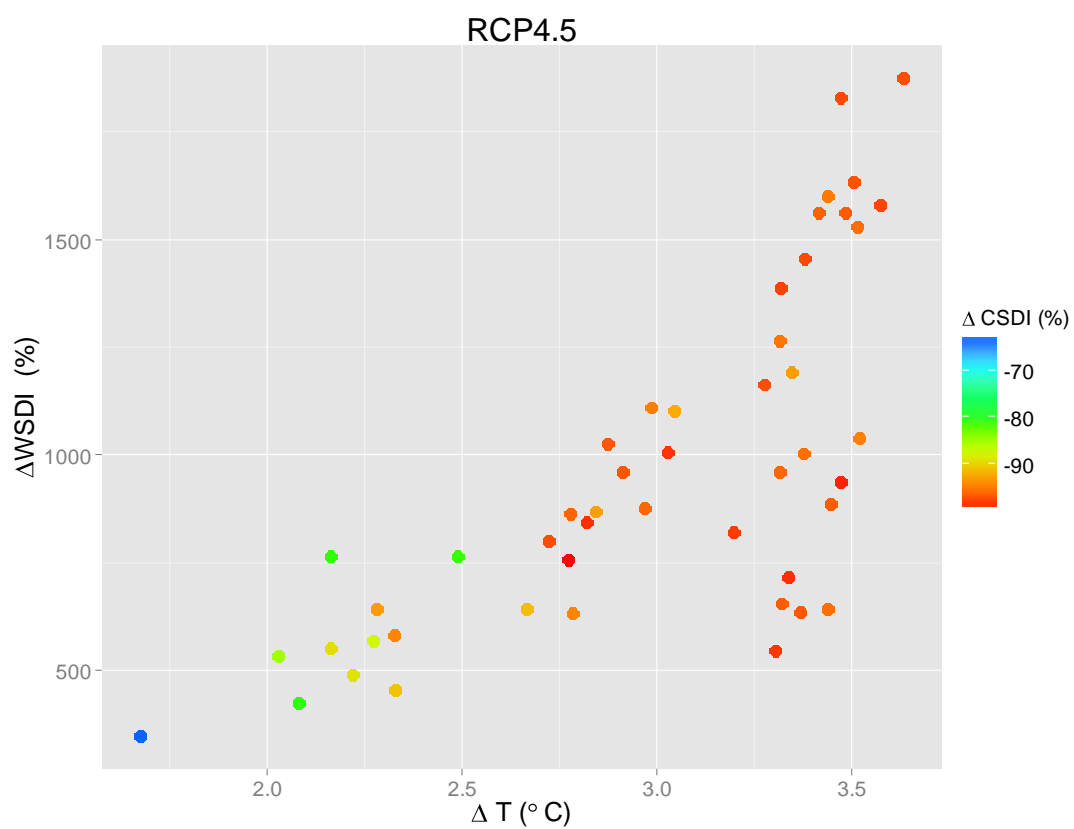


**Figure 9: Changes in mean temperature and changes in temperature extremes indicators for CMIP5 RCP4.5 models**



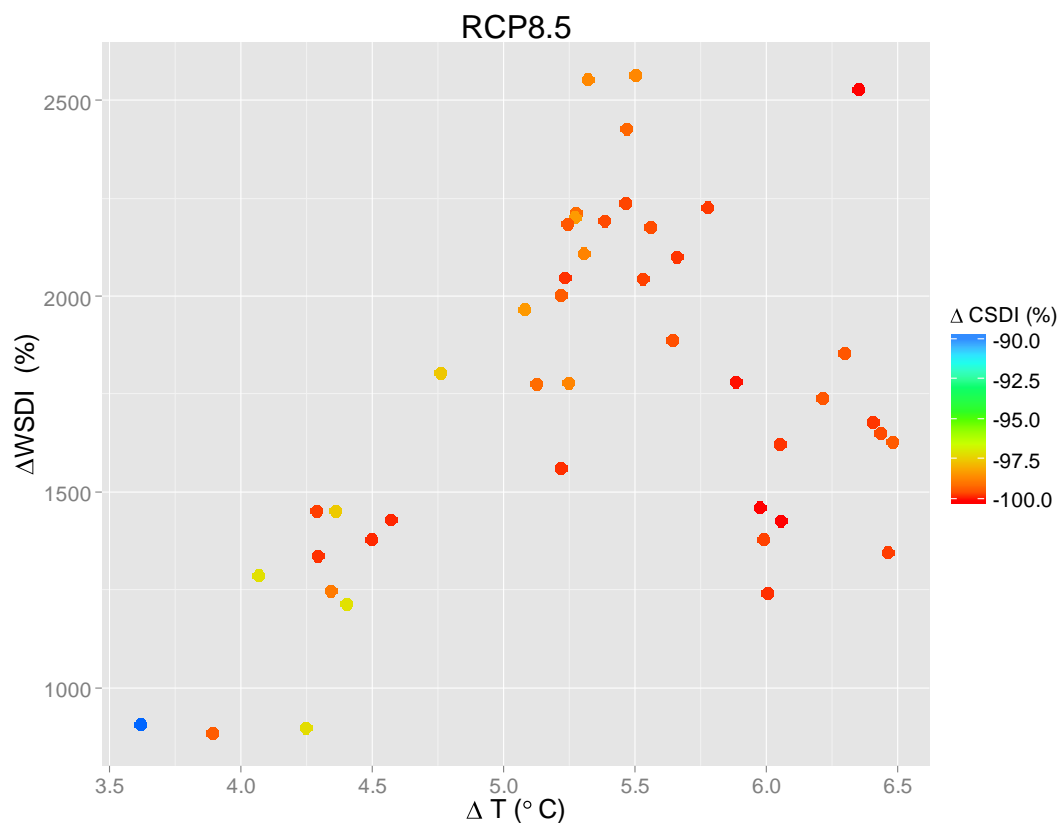


**Figure 10: Changes in mean temperature and changes in temperature extremes indicators for CMIP5 RCP8.5 models**

A clear relationship can be seen between projected changes in mean air temperature and the changes in the indices for temperature extremes (Figure 9 and Figure 10). Model runs projecting large increases in mean air temperature in general also project the largest increase in warm spell duration and largest decrease in cold spell duration. However, for both RCPs the variation in changes in the warm spell duration index is large between the models projecting largest changes in mean air temperature. Note that all model runs project strong increases in warm spells and strong decreases in cold spells. The figures in Appendix: Changes in indices for climatic extremes list the projected changes in climatic extremes indicators for all ensemble members included in the database by [Sillmann *et al.*, 2013a].

**The selection of models resulting from the initial selection based on changes in mean (section 4.2,**

**Table 4) is further refined based on the available data on extremes. The models are selected based on the climate indices that are most appropriate for the corner of the ensemble in which the models are located (**

Table 6). For example for the warm and dry projection, the ETCCDI index for extremes in heat (WSDI: warm spell duration index) and the ETCCDI index for extreme droughts (CDD: consecutive dry days) are leading.

**Table 6: ETCCDI indices leading the selection based on extremes.**

Projection	ETCCDI indices leading selection
Warm, Dry	WSDI, CDD
Warm, Wet	WSDI, R99pTOT
Cold, Wet	CSDI, R99pTOT



For both indices the models are assigned scores descending from 5 to 1 according to their ranking (1 to 5) for that index. For example for the CMCC-CM\_r1i1p1 model in the warm, dry corner for RCP4.5, the rank for  $\Delta WSDI$  is 2<sup>nd</sup>, resulting in a score of 4 and the rank  $\Delta CDD$  is 2<sup>nd</sup>, resulting in a score of 4 as well. The scores for the ETCCDI index related to temperature and the ETCCDI index related to precipitation are averaged to obtain a combined score. The two models with the highest combined scores are selected.

Figure 11 and Figure 12 shows the results of the scoring and the final selection selection for RCP4.5 model runs and RCP8.5 model runs respectively. For both RCPs the initial selection of 20 model runs is reduced to 8 model runs after the refined selection.

RCP	Projection	model	$\Delta R99P$ (%)	$\Delta CDD$ (%)	$\Delta WSDI$ (%)	$\Delta CSDI$ (%)	$\Delta T$ (°C)	$\Delta P$ (%)	T index rank	P index rank	Combined score
RCP4.5	Warm, dry	CMCC-CM_r1i1p1	98.3	10.5	1162.5	-97.1	3.3	4.2	4	4	4.0
RCP4.5	Warm, dry	CMCC-CMS_r1i1p1	56.9	14.3	938.2	-98.4	3.5	-2.9	2	5	3.5
RCP4.5	Warm, dry	IPSL-CM5A-LR_r2i1p1	72.2	4.8	886.1	-96.3	3.4	3.1	1	3	2.0
RCP4.5	Warm, dry	IPSL-CM5A-LR_r3i1p1	72.9	3.8	961.0	-96.0	3.3	6.2	3	2	2.5
RCP4.5	Warm, dry	IPSL-CM5A-MR_r1i1p1	75.6	1.4	1472.0	-99.7	3.5	6.2	5	1	3.0
RCP4.5	Warm, wet	CanESM2_r1i1p1	107.0	-10.0	633.9	-96.7	3.4	17.0	1	4	2.5
RCP4.5	Warm, wet	CSIRO-Mk3-6-0_r3i1p1	57.8	-7.5	1600.8	-94.8	3.4	13.3	4	1	2.5
RCP4.5	Warm, wet	CSIRO-Mk3-6-0_r4i1p1	109.3	-9.6	1530.3	-95.4	3.5	15.6	2	5	3.5
RCP4.5	Warm, wet	CSIRO-Mk3-6-0_r5i1p1	87.7	-3.8	1634.4	-96.9	3.5	14.8	5	3	4.0
RCP4.5	Warm, wet	CSIRO-Mk3-6-0_r6i1p1	69.1	-7.8	1563.8	-96.5	3.5	13.5	3	2	2.5
RCP4.5	Cold, wet	bcc-csm1-1_r1i1p1	104.7	-5.6	490.2	-88.8	2.2	14.5	2	4	3.0
RCP4.5	Cold, wet	BNU-ESM_r1i1p1	140.3	-6.7	729.3	-85.9	2.5	12.7	3	5	4.0
RCP4.5	Cold, wet	CCSM4_r2i1p1	66.9	-2.9	531.9	-84.8	2.0	9.7	4	3	3.5
RCP4.5	Cold, wet	CNRM-CM5_r1i1p1	41.9	-0.7	454.2	-90.6	2.3	11.9	1	2	1.5
RCP4.5	Cold, wet	IPSL-CM5B-LR_r1i1p1	35.1	-11.8	424.3	-80.7	2.1	12.9	5	1	3.0
RCP4.5	Cold, dry	bcc-csm1-1-m_r1i1p1	46.1	-2.3	569.3	-87.4	2.3	5.8	2	1	1.5
RCP4.5	Cold, dry	CCSM4_r6i1p1	45.8	5.6	809.9	-88.2	2.2	4.5	1	5	3.0
RCP4.5	Cold, dry	CESM1-BGC_r1i1p1	57.9	4.3	696.0	-85.6	2.1	6.1	3	4	3.5
RCP4.5	Cold, dry	GISS-E2-R_r6i1p1	47.8	-2.2	764.7	-81.0	2.2	4.1	4	2	3.0
RCP4.5	Cold, dry	inmcm4_r1i1p1	10.5	2.9	347.5	-63.4	1.7	2.7	5	3	4.0

selected model

**Figure 11: Projected changes in climatic extremes indicators and mean temperature and precipitation for RCP4.5 model runs selected in section 4.2. Model runs selected for checking to a climatic reference dataset are highlighted orange.**



RCP	Projection	model	$\Delta R99P$ (%)	$\Delta CDD$ (%)	$\Delta WSDI$ (%)	$\Delta CSDI$ (%)	$\Delta T$ (°C)	$\Delta P$ (%)	T index rank	P index rank	Combined score
RCP8.5	Warm, dry	CMCC-CMS_r1i1p1	140.2	24.1	1855.1	-99.4	6.3	-3.1	5	5	5.0
RCP8.5	Warm, dry	IPSL-CM5A-LR_r1i1p1	125.4	3.3	1627.4	-99.3	6.5	3.5	2	1	1.5
RCP8.5	Warm, dry	IPSL-CM5A-LR_r2i1p1	145.7	9.3	1346.7	-99.7	6.5	4.1	1	3	2.0
RCP8.5	Warm, dry	IPSL-CM5A-LR_r3i1p1	143.9	6.4	1679.0	-99.7	6.4	6.9	4	2	3.0
RCP8.5	Warm, dry	IPSL-CM5A-LR_r4i1p1	140.8	13.7	1651.8	-99.5	6.4	3.6	3	4	3.5
RCP8.5	Warm, wet	CanESM2_r1i1p1	219.0	-17.7	1378.5	-99.6	6.0	28.9	2	2	2.0
RCP8.5	Warm, wet	CanESM2_r2i1p1	227.4	-15.2	1623.6	-99.8	6.1	36.9	5	3	4.0
RCP8.5	Warm, wet	CanESM2_r3i1p1	295.5	-11.7	1426.1	-100.0	6.1	37.4	3	5	4.0
RCP8.5	Warm, wet	CanESM2_r4i1p1	192.9	-12.6	1460.6	-100.0	6.0	29.4	4	1	2.5
RCP8.5	Warm, wet	CanESM2_r5i1p1	261.7	-10.1	1242.2	-99.8	6.0	37.0	1	4	2.5
RCP8.5	Cold, wet	bcc-csm1-1_r1i1p1	220.6	-9.6	1215.6	-97.1	4.4	29.7	5	5	5.0
RCP8.5	Cold, wet	CNRM-CM5_r1i1p1	75.6	-3.4	884.7	-99.3	3.9	17.4	2	1	1.5
RCP8.5	Cold, wet	IPSL-CM5B-LR_r1i1p1	88.4	-16.7	897.8	-97.1	4.2	23.4	4	2	3.0
RCP8.5	Cold, wet	MIROC5_r1i1p1	145.3	-12.4	1337.8	-99.8	4.3	17.7	1	3	2.0
RCP8.5	Cold, wet	MRI-CGCM3_r1i1p1	157.0	-12.6	1452.5	-97.4	4.4	22.1	3	4	3.5
RCP8.5	Cold, dry	CCSM4_r1i1p1	112.5	7.9	1451.4	-99.7	4.3	11.0	1	4	2.5
RCP8.5	Cold, dry	CCSM4_r6i1p1	102.8	5.0	1858.5	-98.3	4.2	11.4	4	1	2.5
RCP8.5	Cold, dry	EC-EARTH_r2i1p1	161.6	9.2	1984.5	-99.3	4.4	6.8	2	5	3.5
RCP8.5	Cold, dry	EC-EARTH_r9i1p1	175.7	5.5	1994.2	-98.9	4.3	7.4	3	2	2.5
RCP8.5	Cold, dry	inmcm4_r1i1p1	30.3	5.6	905.6	-89.6	3.6	5.4	5	3	4.0

**Figure 12: Projected changes in climatic extremes indicators and mean temperature and precipitation for RCP8.5 model runs selected in section 4.2. Model runs selected for checking to a climatic reference dataset are highlighted orange.**

#### 4.4 Final selection: Selection based on GCM validation to climatic reference

The models remaining after the refined selection are subjected to a validation to a climatic reference product. For this validation the WFDEI [Weedon *et al.*, 2014] dataset is used. The selected models are compared to WFDEI for six domains (upstream Indus, upstream Ganges, upstream Brahmaputra, downstream Indus, downstream Ganges, downstream Brahmaputra). Criteria to assess each model's ability to simulate the reference climate include comparisons between the model simulation and WFDEI for monthly average mean air temperature and monthly precipitation sums. The analysis described here is a skill assessment of the selected models remaining from section 4.3 for the period 1980-2004. In the end four GCMs are selected for each RCP-scenario.

The output from the GCMs was obtained using the Climate4impact data portal ([www.climate4impact.eu](http://www.climate4impact.eu)). The temporal resolution of the data was monthly and the variables subject to the reality check were precipitation and temperature. After downloading all data a spatial mask was applied to the data so that the climate information was assigned to the right subbasin. Figure 4.4.1 shows the outline of the six subbasins that are used.



### Outline of the 6 subbasins in the HI-AWARE project

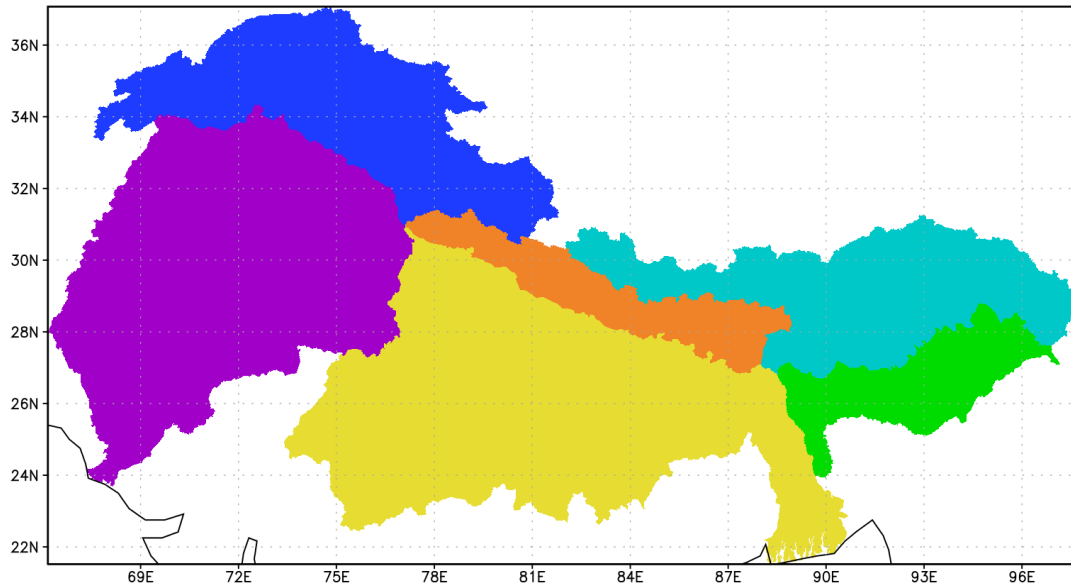


**Figure 13: Outline of the subbasins used in reality checking climate information; purple: lower Indus, dark blue: upper Indus, yellow: lower Ganges, orange: upper Ganges, light blue: upper Brahmaputra, green: lower Brahmaputra.**

#### 4.4.1 Skill Assessment of GCMs 1980-2004

To assess the performance of the selected GCMs skill scores were derived based on earlier work by [Perkins et al., 2007], [Sanchez et al., 2009] and [Kjellström et al., 2010]. The performance of every model to simulate precipitation and temperature are quantified using skill scores. The calculation of temperature and precipitation differ from each other.

For the calculation of the skill score of temperature the approach by [Perkins et al., 2007] is used. A metric was developed which “calculates the cumulative minimum value of two distributions of each binned value, thereby measuring the common area between two PDFs”:

$$S_{score} = \sum_1^n \text{minimum}(Z_{GCM}, Z_{OBS})$$

where n is the number of bins used to calculate the PDF for a given region,  $Z_{GCM}$  is the frequency of values in a given bin from the model, and  $Z_{OBS}$  is the frequency of values in a given bin from the observed data. If a model simulates the observed conditions perfectly, the skill score ( $S_{score}$ ) will equal one, which is the total sum of the probability at each bin center in a given PDF.

The skill score of precipitation is based on the work of [Sanchez et al., 2009] which consists of a collection of 5 skill score functions taking into effect different aspects of the behavior of precipitation, such as “the distribution as a whole in terms of mean (f4) and total area (f1), precipitation for more intense precipitation in the upper (f2) and moderate precipitation (f3) in the lower half of the distribution and the width of the of the distribution through the variance (f5).



The skill score functions as described by [Sanchez *et al.*, 2009] are displayed below for our case of comparing GCM data to the WFDEI dataset.

$$f_1 = 1 - \left( \frac{|A_{GCM} - A_{WFDEI}|}{2 \cdot A_{WFDEI}} \right)^{0.5}$$

$$f_2 = 1 - \left( \frac{|A^+_{GCM} - A^+_{WFDEI}|}{2 \cdot A^+_{WFDEI}} \right)^{0.5}$$

$$f_3 = 1 - \left( \frac{|A^-_{GCM} - A^-_{WFDEI}|}{2 \cdot A^-_{WFDEI}} \right)^{0.5}$$

$$f_4 = 1 - \left( \frac{|\overline{P}_{GCM} - \overline{P}_{WFDEI}|}{2 \cdot \overline{P}_{WFDEI}} \right)^{0.5}$$

$$f_5 = 1 - \left( \frac{|\sigma_{GCM} - \sigma_{WFDEI}|}{2 \cdot \sigma_{WFDEI}} \right)^{0.5}$$

$A_{GCM}$  and  $A_{WFDEI}$  are the areas below the cumulative distribution functions of the GCMs and WFDEI respectively,  $A^+$  and  $A^-$  are the corresponding areas to the right and left of the 50<sup>th</sup> percentile.  $P$  is the spatial and temporal average of the precipitation and  $\sigma$  is the standard deviation. The 5 functions are in the end multiplied by each other to give a total skill score for precipitation.

The skill scores for both temperature and precipitation are calculated for the control period and for the 6 subbasins (see Table 7). Following the concept of [Perkins *et al.*, 2007] the average is taken from the skill scores for both temperature and precipitation and these scores are ranked per subbasin. Subsequently, the rankings of the subbasins are summed for each model which then results in a ranking that is tabulated in Table 8.

The analysis until this point is based on the general performance of the model. However, one of the main meteorological phenomena in the area of interest is the monsoon. Figure 15 shows the monthly averaged precipitation simulated by the GCMs for the period 1980-2004 and the observed numbers from the WFDEI dataset for the six subbasins. Most GCMs have difficulty in simulating the right amount of precipitation for the lower basins and most of them underestimate the precipitation in the monsoon period. The representation of monsoonal precipitation is an important issue in HI-AWARE and so it is decided that an extra ranking should be considered based on the forecast of monsoonal precipitation. This skill score consists only of the absolute bias in precipitation of the GCM for the complete monsoon period (June – September). The highest ranked GCM has the smallest absolute bias and the lowest ranked GCM the largest absolute bias.

Finally, the two rankings (general ranking and monsoon ranking) are combined and weighted to reach a final ranking. The weight of the general ranking is 3 and the weight of the monsoonal ranking is 1. The final ranking of the GCMs is displayed in Table 8.



MODEL	PRECIPITATION						TEMPERATURE					
	LI	UI	UB	LB	LG	UG	LI	UI	UB	LB	LG	UG
CMCC-CM_r1i1p1	0.0729668	0.1047292	0.0025936	0.2414792	0.0869156	0.1429347	0.5933	0.5367	0.3833	0.6467	0.6467	0.6400
CMCC-CMS_r1i1p1	<b>0.1239629</b>	0.0616837	0.0090828	<b>0.2443505</b>	0.1478141	<b>0.3653685</b>	<b>0.61</b>	0.5266667	<b>0.65</b>	<b>0.5533333</b>	0.5666667	0.58
CSIRO-Mk3-6-0_r4i1p1	0.0167	0.0942259	<b>0.4136303</b>	<b>0.1856971</b>	0.0599321	0.067821	0.5033333	<b>0.5733333</b>	<b>0.62</b>	0.4133333	0.51	<b>0.6066667</b>
CSIRO-Mk3-6-0_r5i1p1	0.0240097	0.1169569	<b>0.2943247</b>	0.1698927	0.0573662	0.0645197	0.4966667	<b>0.5533333</b>	<b>0.64</b>	0.4	0.49	0.5566667
BNU-ESM_r1i1p1	<b>0.3228477</b>	0.1546294	0.0367076	0.096209	<b>0.2290518</b>	<b>0.2908699</b>	0.6033333	0.53	<b>0.5666667</b>	0.3966667	0.5966667	0.4266667
CCSM4_r2i1p1	0.0596846	0.0729689	0.0186365	<b>0.203921</b>	<b>0.2687328</b>	0.0239265	<b>0.72</b>	0.4933333	0.4733333	<b>0.5533333</b>	<b>0.6466667</b>	<b>0.6233333</b>
CESM1-BGC_r1i1p1	0.0712663	0.0806376	0.0150762	<b>0.2267536</b>	<b>0.2636944</b>	0.0286206	<b>0.7466667</b>	0.5	0.5	<b>0.59</b>	<b>0.6633333</b>	<b>0.6266667</b>
inmcm4_r1i1p1	<b>0.1362865</b>	<b>0.3572551</b>	<b>0.370019</b>	0.1518801	<b>0.2424004</b>	<b>0.206475</b>	0.5233333	0.4466667	0.4133333	0.27	0.5066667	0.5866667
IPSL-CM5A-LR_r4i1p1	0.0639593	0.0973105	<b>0.2898641</b>	0.0469785	0.0745459	<b>0.4114888</b>	<b>0.61</b>	<b>0.58</b>	0.4266667	<b>0.6866667</b>	<b>0.61</b>	<b>0.66</b>
CanESM2_r2i1p1	<b>0.0810883</b>	<b>0.1637048</b>	0.1860854	0.1310633	<b>0.1555231</b>	0.1067704	0.4966667	0.5066667	<b>0.5233333</b>	0.33	0.5866667	0.5366667
CanESM2_r3i1p1	<b>0.1389739</b>	0.155951	0.1977148	0.1263055	0.1146301	0.1217153	0.5466667	0.46	0.52	0.32	<b>0.6266667</b>	<b>0.5833333</b>
bcc-csm1-1_r1i1p1	0.0562698	<b>0.5696283</b>	<b>0.246664</b>	0.1189422	0.0825863	0.0937898	<b>0.6133333</b>	<b>0.5566667</b>	<b>0.52</b>	0.4266667	<b>0.5633333</b>	0.5233333
MRI-CGCM3_r1i1p1	0.0433584	<b>0.2604017</b>	0.0994176	0.0525369	0.0283097	0.1608897	0.48	0.4533333	0.4133333	<b>0.5866667</b>	0.5	<b>0.5666667</b>
EC-EARTH_r2i1p1	0.010461	<b>0.2729019</b>	0.2011341	0.1350877	0.095489	<b>0.6297115</b>	0.5133333	0.3866667	0.4733333	0.3566667	0.4	0.45

**Table 7: Skill scores of the models for both temperature and precipitation for the 6 subbasins based on skill score analysis (LI: Lower Indus, UI: Upper Indus, UB: Upper Brahmaputra, LB: Lower Brahmaputra, LG: Lower Ganges, UG: Upper Ganges).**



MODEL	LI	UI	UB	LB	LG	UG	TOTAL	RANK	RANK MONSOON	TOTAL RANK
CMCC-CM_r1i1p1	8	10	14	1	7	5	45	7	7	6
CMCC-CMS_r1i1p1	4	12	9	3	8	3	39	5	4	4
CSIRO-Mk3-6-0_r4i1p1	14	8	1	7	11	9	50	10	8	10
CSIRO-Mk3-6-0_r5i1p1	13	7	2	8	12	13	55	14	9	14
BNU-ESM_r1i1p1	1	4	10	10	3	7	35	2	3	1
CCSM4_r2i1p1	3	14	13	4	2	11	47	8	13	9
CESM1-BGC_r1i1p1	2	13	11	2	1	10	39	5	10	5
inmcm4_r1i1p1	9	2	3	14	4	4	36	3	2	2
IPSL-CM5A-LR_r4i1p1	6	5	6	5	9	2	33	1	12	3
CanESM2_r2i1p1	10	6	7	12	5	12	52	12	5	12
CanESM2_r3i1p1	5	11	5	13	6	8	48	9	6	8
bcc-csm1-1_r1i1p1	7	1	4	9	10	14	45	7	11	7
MRI-CGCM3_r1i1p1	12	3	12	6	13	6	52	12	14	13
EC-EARTH_r2i1p1	11	9	8	11	14	1	54	13	1	11
CMCC-CMS_r1i1p1	4	12	9	3	8	3	39	5	4	4
inmcm4_r1i1p1	9	2	3	14	4	4	36	3	2	2

**Table 8: ranking of the models for the 6 subbasins (LI: Lower Indus, UI: Upper Indus, UB: Upper Brahmaputra, LB: Lower Brahmaputra, LG: Lower Ganges, UG: Upper Ganges).  
SS P: Skill Score Precipitation, SS T: Skill Score Temperature**

This ranking will result in the selection of the models. Note that this way of selecting GCMs will omit GCMs which have a very good skill for certain sub-basins, like for example EC-EARTH\_r2i1p1 for the Upper Ganges. Table 9 shows the final selected models following the skill score assessment explained in this paragraph and maintaining the four corners mentioned before. The GCMs which were pre-selected for the warm-wet corner are the models which do a lesser job in simulating the present climate. For the warm-wet corner in the RCP4.5 scenario the GCM had to be selected which is only ranked 10 in the overall final ranking. Another striking feature is that two models (inmcm4\_r1i1p1 and CMCC-CMS\_r1i1p1) are selected for further downscaling for both the RCP4.5 and RCP8.5 scenario.

**Table 9: The selected models based on the skill score analysis**

General Circulation Model	RCP4.5	RCP8.5
BNU-ESM_r1i1p1	x	cold,wet
inmcm4_r1i1p1	x	cold,dry
CMCC-CMS_r1i1p1	x	warm, dry
CSIRO-Mk3-6-0_r4i1p1	x	warm, wet
inmcm4_r1i1p1		x cold, dry
CMCC-CMS_r1i1p1		x warm, dry
bcc-csm1-1_r1i1p1		x cold, wet
CanESM2_r3i1p1		x warm, wet

After this selection an analysis was done on the annual cycle to check if the selected models capture the annual cycle correctly. Figure 14 and Figure 15 show the monthly average of temperature and monthly average of precipitation respectively for each subbasin. The selected models are dark red in color and the other models are light red in color. As could be expected a large difference between all models is witnessed. Figure 14 shows that all GCMs are doing a poor job in simulating the temperature in wintertime for the Upper Indus. The annual cycle of precipitation is even harder for the GCMs to simulate. Especially in the Upper Indus, the models don't agree with each other about the annual cycles. The spread between models is large but there is reasonable agreement for most of the subbasins. As mentioned before, most GCMs underestimate the precipitation in the lower subbasins.

One of the shortcomings of the presented analysis is that GCMs are selected on their overall performance over a climatological period and not on properties like timing of the monsoon season. Also, models vary in their skill per subbasin as EC-EARTH\_r2i1p1 shows with a high skill for temperature in the Upper Ganges, but having difficulties in the other subbasins. The analysis on the annual cycles show that the selected models are on average correctly selected.



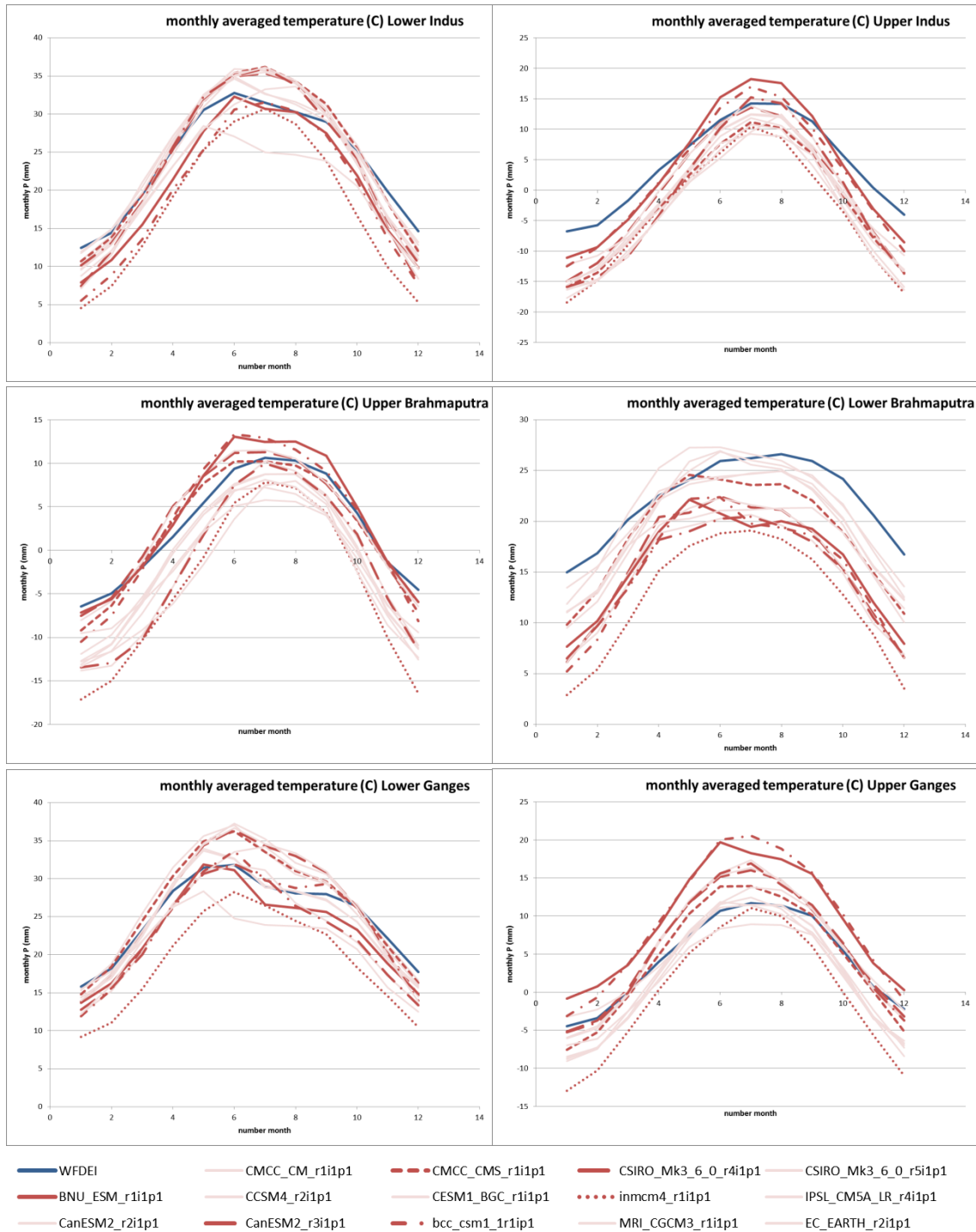
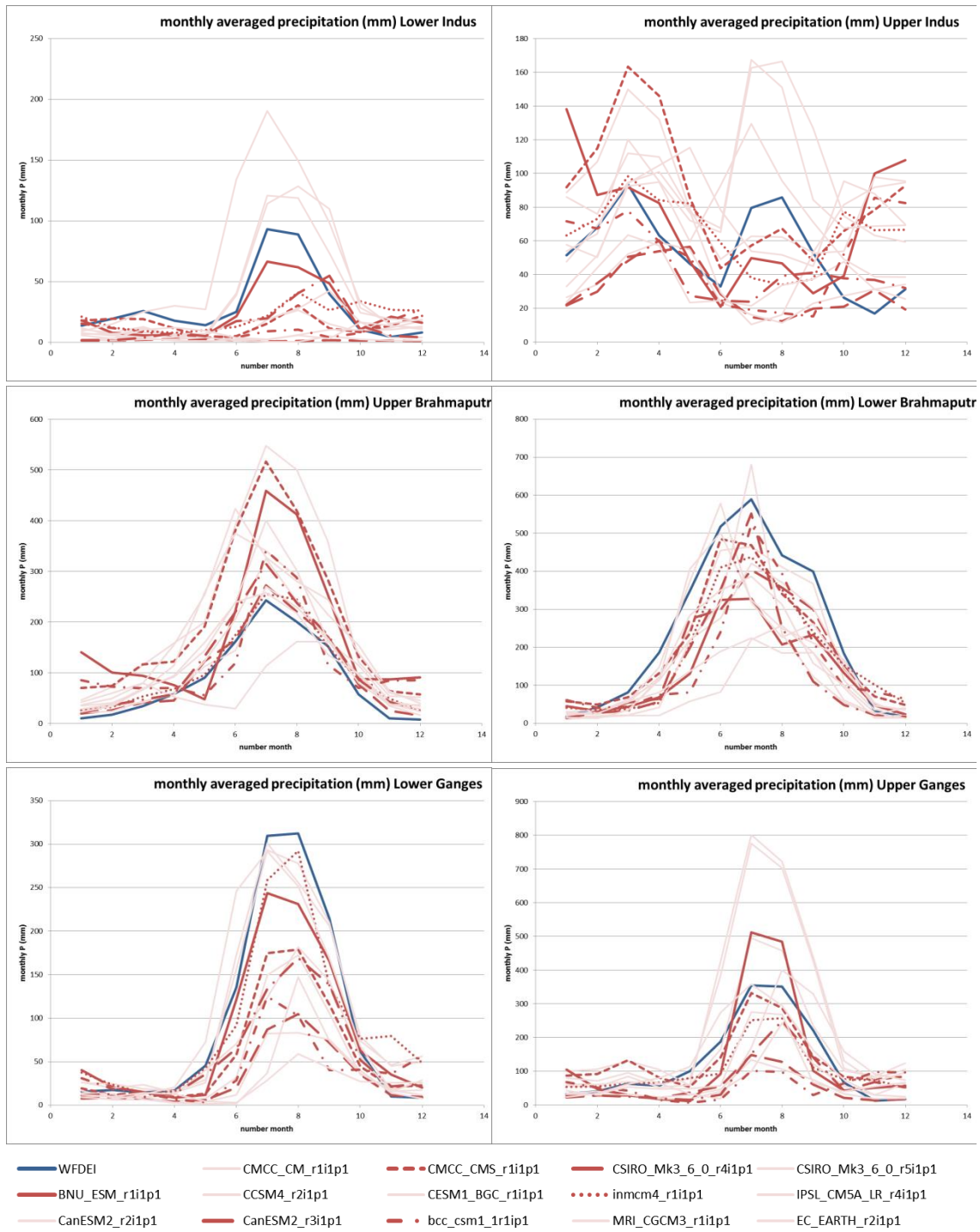


Figure 14: Average annual cycles of temperature (C) per GCM and per subbasin (red: selected GCMs, light red: not selected GCMs) and WFDEI (blue).





**Figure 15: Average annual cycles of precipitation (mm) per GCM and per subbasin (red: selected GCMs, light red: not selected GCMs) and WFDEI (blue).**



# 5 Statistical Downscaling

Since the venture of General Circulation Models (GCMs), statistical downscaling techniques have been developed to account for the scale differences between GCMs and hydrological models, and to interpolate regional scale atmospheric predictor variables to station-scale meteorological series [Karl *et al.*, 1990; Hay *et al.*, 1991]. GCMs typically operate at multiple degrees spatial resolution, but applications like hydrological models, forced by the data from GCMs, operate at higher resolutions, up to several meters. Many processes, such as circulation patterns leading to hydrological extreme events cannot be resolved by GCMs [Christensen and Christensen, 2002]. In HIAWARE, the used models operate at spatial resolutions around 5-10 km, thus also requiring downscaling of the GCM data. Given the mountainous nature of the upstream parts of the Indus, Ganges and Brahmaputra (IGB) basins, preferably a downscaling technique is used that has proven its usefulness under these conditions. A first prerequisite for a successful downscaling of future climate is to have a high-quality high-resolution dataset of the historical climate, which can be used as a baseline for the downscaling, when combined with data from GCMs (Figure 16). Differences between past and future climate in the low-resolution GCM data are downscaled to high resolution using the historical baseline climate dataset.

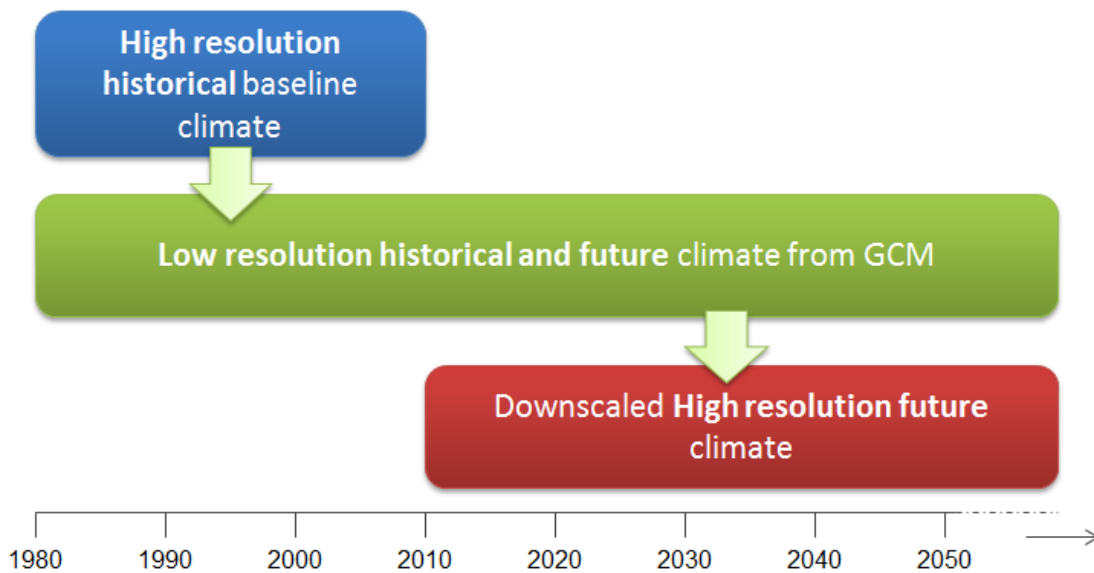


**Figure 16: High-resolution historical climate data is combined with low resolution GCM data to generate high resolution future climate data.**

## 5.1 Historical baseline climate dataset

### 5.1.1 Existing gridded meteorological forcing datasets

Understanding the spatial and temporal variability of precipitation in mountainous areas remains a key challenge. Point measurements are often not sufficient to capture the strong gradients in the multiple local factors that determine the distribution of precipitation. Climatologists have created numerous gridded datasets, based on observations. Since many of the existing gridded data products include precipitation and temperature at near surface level, they can be used to overcome data gaps in observations.



A distinction in two groups can be made regarding gridded datasets for temperature and precipitation: (i) datasets based created using advanced geo-statistical interpolation techniques based on station observations, and (ii) datasets based on blending of climate model output and observations (often referred to as reanalysis products). A tabular overview of available datasets in the IGB and their key characteristics is provided in Table 10. Apart from differences in the underlying methodology (interpolation of observations or reanalysis) the main differences in the datasets are the spatial resolution, temporal resolution and time span covered.

**Table 10: Overview of gridded meteorological products.**

Dataset	Type	Coverage	Resolution	Frequency	Period	Parameters	Institute
<b>NCEP/NCAR reanalysis data</b>	Re-analysis	Global	~209 km (T62 grid)	6 hourly	1948 - present	Prec, Tmax, Tmin, Tavg ( + many more)	NCEP/NCAR
<b>CFSR</b>	Re-analysis	Global	~ 50 km (0.5 degree)	1 hourly, 6 hourly, monthly	1979-2010	Prec, Tmax, Tmin, Tavg ( + many more)	NCEP
<b>ERA 15 basic</b>	Re-analysis	Global	basic: ~ 250 km (2.5 degrees)	monthly	1979 - 1994	Prec, Tmax, Tmin, Tavg ( + many more)	ECMWF
<b>ERA 15 advanced</b>	Re-analysis	Global	~ 120 km (N80 grid)	monthly	1979 - 1994		ECMWF
<b>ERA 40 basic</b>	Re-analysis	Global	~ 250 km (2.5 degrees)	6 hourly	1957 - 2002	Prec, Tmax, Tmin, Tavg ( + many more)	ECMWF
<b>ERA 40 advanced</b>	Re-analysis	Global	~ 120 km (N80 grid)	6 hourly	1957 - 2002	Prec, Tmax, Tmin, Tavg ( + many more)	ECMWF
<b>ERA Interim</b>	Re-analysis	Global	~ 70 km (N128 grid)	6 hourly	1979 - present	Prec, Tmax, Tmin, Tavg ( + many more)	ECMWF
<b>ERA 20 CM</b>	Climate model ensemble	Global	~ 120 km (N80 grid)	3 hourly	1900-2009	Prec, Tavg	ECMWF
<b>NASA MERRA</b>	Re-analysis	Global	~ 70 km (0.5 x 0.67 degrees))	3 hourly	1979 - present	Prec, Tmax, Tmin, Tavg ( + many more)	NASA
<b>Global Meteorological Forcing Dataset for land surface modeling</b>	Re-analysis + observations	Global	~ 50 km (0.5 degree)	3 hourly	1948 - 2008	Prec, Tmax, Tmin, Tavg ( + many more)	Princeton University
<b>APHRODITE</b>	Observations	Asia	~ 25 km (0.25 degree)	Daily	1961 - 2007	Prec, Tavg	Meteorological Research Institute of Japan Meteorological Agency
<b>CRU TS 3.10.01</b>	Observations	Global	~ 50 km (0.5 degree)	Monthly	1901-2009	Prec, Tmax, Tmin, Tavg ( + many more)	Climate Research Unit at the University of East Anglia
<b>GPCC</b>	Observations	Global	~ 50 km (0.5 degree)	Monthly	1901-2007	Precipitation	Global Precipitation Climatology Centre
<b>GPCP</b>	Observations	Global	~ 250 km (2.5 degree)	Monthly	1979 -	Precipitation	GEWEX



<b>CPC-UGBAGDP</b>	Observations	Global	degrees) ~ 50 km (0.5 degree)	Daily	present 1979- present	Prec	CPC
<b>DEL</b>	Observations	Global	~ 50 km (0.5 degree)	monthly	1900- 2008	Prec, Tair	CCR Univ of Delaware
<b>HAR</b>	WRF-model coupled to ERA- INTERIM	High Asia	10 km	hourly	2000- 2012	Prec, Tair, many others	TU Berlin

A thorough comparison on the performance of existing gridded products for the HKH region [Palazzi *et al.*, 2013] highlights the striking differences between the different products. All the analyzed products are subject to limited spatial resolution. They are mostly suitable for large-scale continental studies. However, to analyse climate variations at smaller scales and in orographically complex regions, such as the IGB, they lack accuracy.

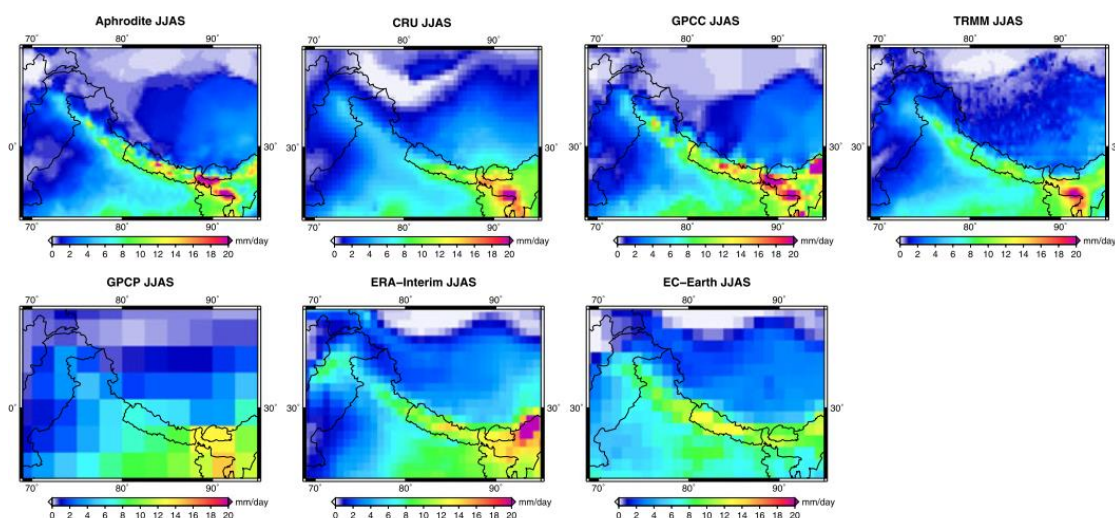


**Figure 17: Multiannual mean (1998-2007) of summer (JJAS) precipitation over the HKKH region as represented by different dataset [Palazzi *et al.*, 2013].**

Researches who compared the performance of TRMM and APHRODITE over Nepal concluded that the latter is the more accurate dataset [Duncan and Biggs, 2012]. Other researchers also concluded that there is large variability in performance between different gridded products by comparing them for multiple transects crossing the Himalayan ranges [Andermann *et al.*, 2011]. They also conclude that APHRODITE, based on ground station data solely, gives the best precipitation estimates. However, they also mention that the lack of stations at high elevations limits the accuracy of this dataset. A study for the Upper Indus basin, also showed that high altitude precipitation in APHRODITE is strongly underestimated [Lutz *et al.*, 2014b]. [Immerzeel *et al.*, 2015] compared four precipitation products for the Upper Indus basin and validated them to observed river discharge. According to their analysis, ERA-Interim provides the best estimate of precipitation in terms of annual totals.



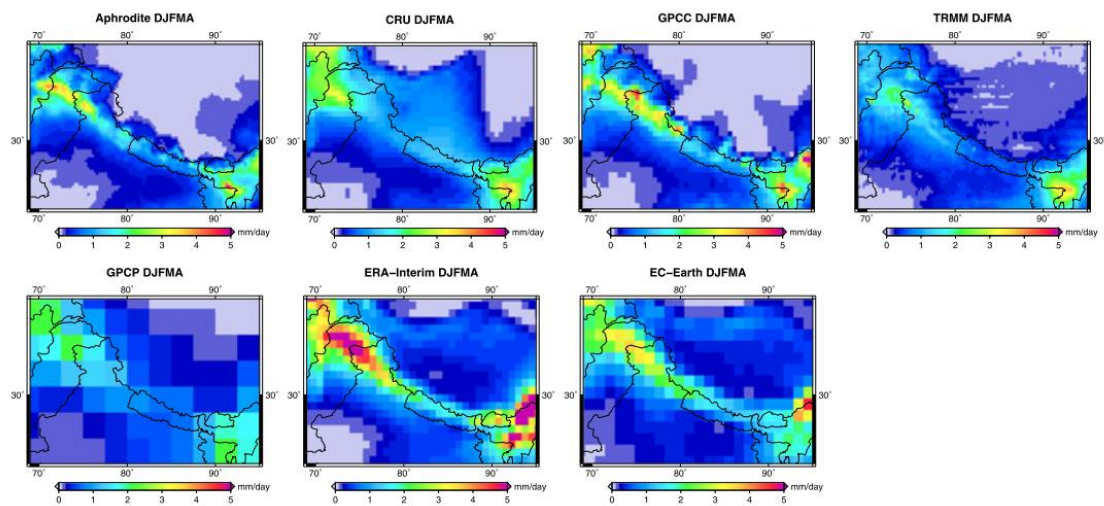


Figure 18: Multiannual mean (1998-2007) of winter (DJFMA) precipitation over the HKH region as represented by different dataset [Palazzi *et al.*, 2013].

In 2014, the Refined High Asian Reanalysis (HAR) was released [Maussion *et al.*, 2014]. HAR is based on WRF model runs with an hourly time step, which are bounded daily to the ERA-INTERIM dataset. Although the product has a high spatial (10 km) and temporal (1 h) resolution, it covers a relatively short time range (2000-2012), and does not cover the entire IGB.

### 5.1.2 Station observations

Station observations in the upstream parts of the IGB basins are sparse. Figure 19 and Table 11 list the stations and station metadata, including record length, as available in this project. As evident from the map, the stations are very unequally distributed over the basin and mostly located in the valleys. As can be seen in the table, eight out of forty stations are located above 4000 m a.s.l., with the highest being located at an elevation of 4730 m a.s.l. In addition, many stations have rather short records available.

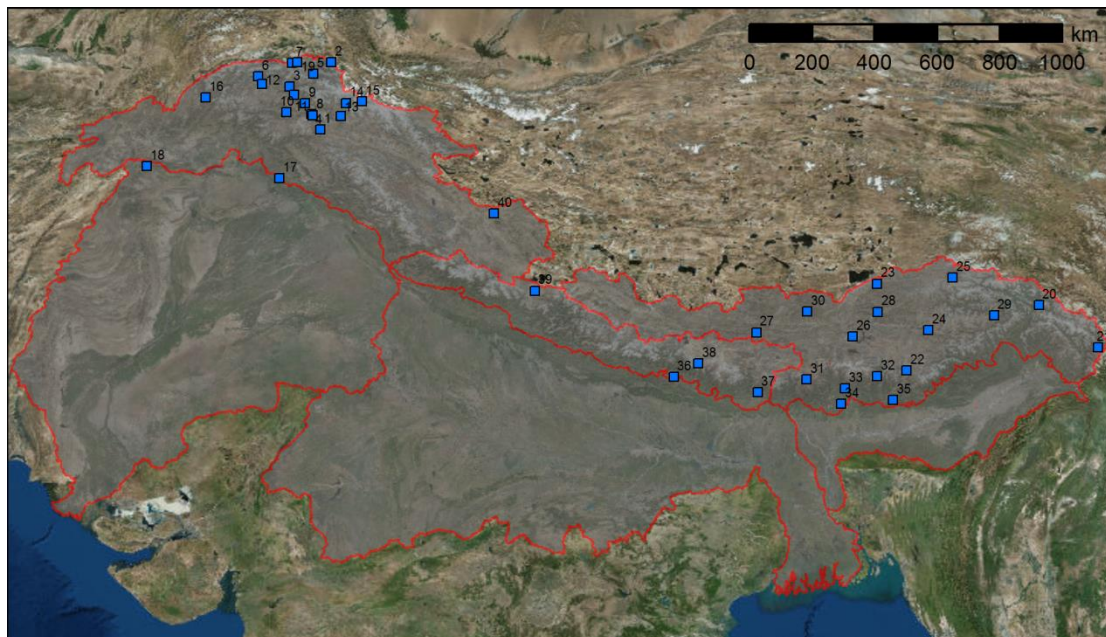


Figure 19: Locations of meteorological stations in the upper IGB basins.



**Table 11: Meteorological ground station records in the upper IGB used in HIAWARE.**

ID	Name	Source	Lon (dd)	Lat (dd)	Elevation (m asl)	StartDate	EndDate
1	Burzil	WAPDA	75.088	34.911	4030	01/01/2000	31/12/2008
2	Khunjerab	WAPDA	75.400	36.850	4730	01/01/2000	31/12/2008
3	Naltar	WAPDA	74.189	36.158	2810	01/01/2000	31/12/2008
4	Rama	WAPDA	74.817	35.367	3000	01/01/2000	31/12/2008
5	Rattu	WAPDA	74.871	36.515	2570	01/01/2000	31/12/2008
6	Yasin	WAPDA	73.300	36.450	3150	01/01/2000	31/12/2008
7	Ziarat	WAPDA	74.276	36.836	3669	01/01/2000	31/12/2008
8	Astore	PMD	74.857	35.329	2168	01/01/2000	31/12/2005
9	Bunji	PMD	74.633	35.667	1470	01/01/2000	31/12/2005
10	Chilas	PMD	74.100	35.417	1251	01/01/2000	31/12/2005
11	Gilgit	PMD	74.333	35.917	1459	01/01/2000	31/12/2005
12	Gupis	PMD	73.400	36.230	2156	01/01/2000	31/12/2005
13	Skardu	PMD	75.680	35.300	2210	01/01/2000	31/12/2005
14	Askole	PMD	75.815	35.681	3015	10/08/2005	31/12/2007
15	Urdukas	PMD	76.286	35.728	3927	06/17/2004	31/12/2007
16	Chitral	PMD	71.780	35.839	1500	01/01/2000	01/01/2005
17	Kotli	PMD	73.900	33.520	2017	01/01/2000	01/01/2005
18	Parachinar	PMD	70.083	33.867	1726	01/01/2000	01/01/2005
19	Khunjerab	Winiger/ICIMOD	74.417	36.850	4700	01/01/2000	12/31/2012
20	Bomi	ICIMOD	95.76	29.86	2736	01/01/2000	12/31/2006
21	Chayu	ICIMOD	97.46	28.65	2327.6	01/01/2000	12/31/2006
22	Cuona	ICIMOD	91.95	27.98	4280	01/01/2000	12/31/2006
23	Dangxiong	ICIMOD	91.1	30.48	4200	01/01/2000	12/31/2006
24	Jiacha	ICIMOD	92.58	29.15	3260	01/01/2000	12/31/2006
25	Jiali	ICIMOD	93.28	30.66	4488.8	01/01/2000	12/31/2006
26	Langkazi	ICIMOD	90.4	28.96	4431.7	01/01/2000	12/31/2006
27	Lazi	ICIMOD	87.63	29.08	4000	01/01/2000	12/30/2005
28	Lhasa	ICIMOD	91.13	29.67	3648.7	01/01/2000	12/31/2006
29	Linshi	ICIMOD	94.47	29.57	3000	01/01/2000	12/31/2006
30	Namulin	ICIMOD	89.1	29.68	4000	01/01/2000	12/31/2006
31	Pali	ICIMOD	89.08	27.73	4300	01/01/2000	12/31/2006
32	Dungkhar	ICIMOD	91.1	27.82	2010	01/01/2000	12/31/2006
33	Phobjekha	ICIMOD	90.18	27.47	2860	01/01/2000	12/31/2006
34	Sunkosh	ICIMOD	90.07	27.02	410	01/01/2000	12/31/2006
35	Wamrong	ICIMOD	91.57	27.13	2180	01/01/2000	12/31/2006
36	Kakani	ICIMOD	85.25	27.8	2064	01/01/2000	12/31/2009
37	Taplejung	ICIMOD	87.66667	27.35	1732	01/01/2000	12/31/2010
38	Nielamu	ICIMOD	85.96	28.18	3310	01/01/2000	12/31/2006
39	Pulan	ICIMOD	81.25	30.28	3900	01/01/2000	12/31/2006
40	Shiquanhe	ICIMOD	80.08	32.5	4278	01/01/2000	12/31/2006



### 5.1.3 New historical baseline climate dataset for the IGB basins

Given the results from the cited comparison studies, ERA-INTERIM data will be used as basis to construct a historical baseline climate dataset for the upstream, mountainous parts of the IGB, spanning 30 years, from 1 January 1981 to 31 December 2010, at a daily time step. The temperature data will be downscaled from 0.75° to 5 km spatial resolution using a high-resolution DEM and temperature lapse rates, and bias-corrected using the available meteorological station observations. The precipitation data will be corrected using observed glacier mass balance data, according to the methodology developed in [Immerzeel *et al.*, 2012, 2015]. Based on geodetic measurements of glacier mass balance [Gardelle *et al.*, 2012, 2013], precipitation gradients are calculated to improve and downscale the ERA-INTERIM precipitation fields. The same datasets will be used for the downstream parts of the IGB, but no correction to precipitation fields based on observed glacier mass balance will be made, since this is only applicable to the high mountain environment.

Since the amounts of precipitation in the ground station data and gridded product are underestimated it is very likely that the precipitation necessary to supply the observed amount of discharged water is occurring at high altitudes. Research in this area [“Batura Investigations Group,” 1979; Hewitt, 2005, 2007a, 2011; Winiger *et al.*, 2005] suggests that precipitation increases up to 5000 to 6000 m a.s.l., where it is at its maximum, and decreases at higher altitudes (Figure 20, right panel).

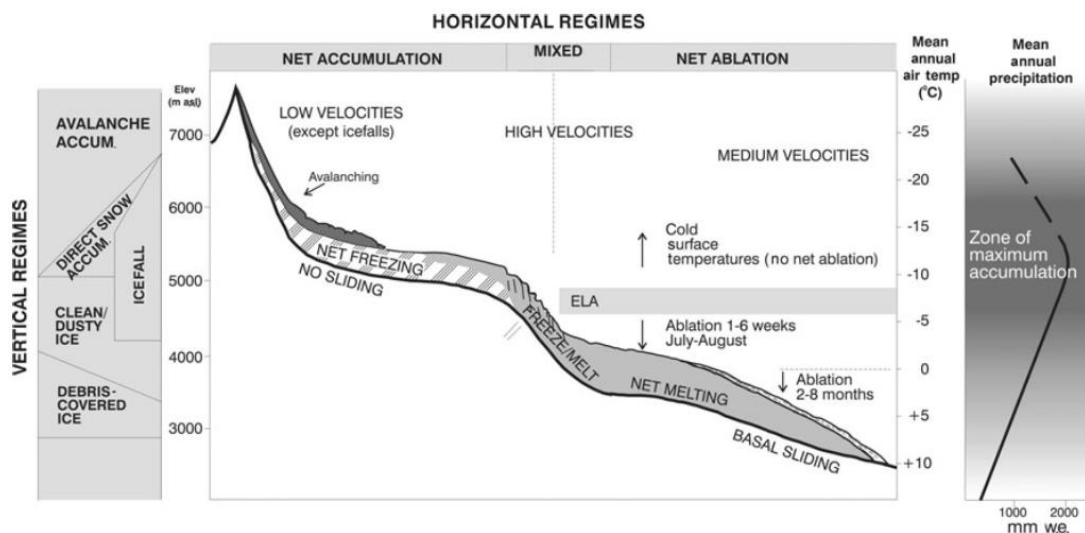


**Figure 20: Conceptual model of vertical and horizontal meteorological and cryospheric regimes in the Karakoram [Hewitt, 2007b].**

In the construction of an improved gridded meteorological dataset for the upper IGB basins we assume this conceptual model to be correct to infer vertical precipitation lapse rates based on a linear increase of precipitation from a certain reference elevation (HREF) up to an elevation of maximum precipitation (HMAX) and decreasing linearly at higher altitudes with the same lapse rate [Immerzeel *et al.*, 2012, 2015].

In summary, the methodology to improve the data for air temperature and precipitation is as follows:

- ERA-INTERIM air temperature and precipitation data are used as basis



- Air temperature (step 1):
  - Temperature fields are initially corrected using daily determined temperature lapse rates
  - The bias between ground observations and ERA-INTERIM is determined
  - A monthly bias averaged over the available stations is derived
  - Temperature fields are corrected using the monthly bias
- Precipitation (step 2):
  - Using the downscaled and bias-corrected temperature fields (result of step 1), the observed glacier mass balance is included as a proxy to derive local precipitation lapse rates
  - Local precipitation lapse rates are spatially interpolated
  - Spatially interpolated field of precipitation lapse rates is used to spatially interpolated ERA-INTERIM precipitation grids

#### 5.1.4 Correction of air temperature

As a first step, the ERA-INTERIM air temperature fields are downscaled from 0.75° original resolution to 1 km resolution by applying a daily derived temperature lapse rate to correct for elevation differences between a DEM at 1 km resolution and a DEM at 0.75° resolution representing the average elevation of ERA-INTERIM grid cells and bias-correction using ground station data. The vertical temperature lapse rate is largely dependent on the moisture content of the air and generally varies between the dry adiabatic lapse rate ( $-0.0098\text{ }^{\circ}\text{C m}^{-1}$ ) and the saturated adiabatic lapse rate (typically  $-0.005\text{ }^{\circ}\text{C m}^{-1}$ , strongly dependent on the temperature). Thus, vertical temperature lapse rates tend to be steeper during dry periods and less steep during wet periods, such as the monsoon. For each day we determine the temperature lapse rate by calculating an average temperature lapse rate from the air temperature values at the original ERA-INTERIM grid cells and their elevations. Figure 21 shows the lapse rates determined for the year 1999, and demonstrates that the less steep lapse rates during the monsoon month (June-September) are nicely represented as well as the steeper lapse rates during the dryer periods.

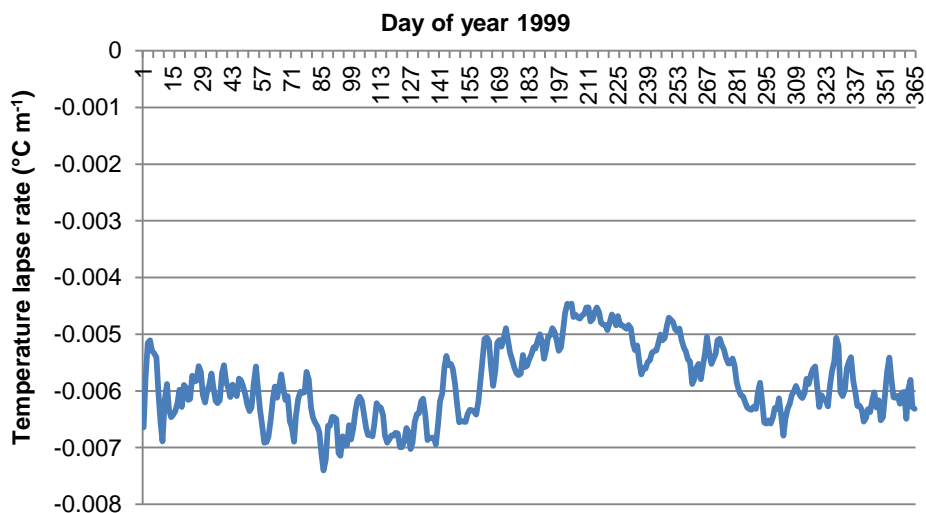


**Figure 21: Average temperature lapse rates in 1999 in the upper IGB basins daily calculated from the ERA-INTERIM grid cells and their elevations, covering the upper IGB.**



Subsequently, the temperature bias between the ground stations and the temperature grids are determined, for stations with records covering parts of the period 2000-2010. Stations which location could not be verified, or the elevation difference between the elevation provided in the station's metadata and its elevation according to the 1km resolution DEM exceeds 400 meters are omitted (11 stations, IDs: 4, 16, 17, 18, 21, 25, 32, 35, 36, 38, 39), 29 stations are used for the bias-correction. In Figure 22, the bias is plotted for twelve months along with the station's altitude. From the figure no significant relation between the bias and elevation can be determined (blue lines). Therefore the average bias of the 29 stations (blue dots) is used for each month to bias-correct the downscaled ERA-INTERIM temperature fields.

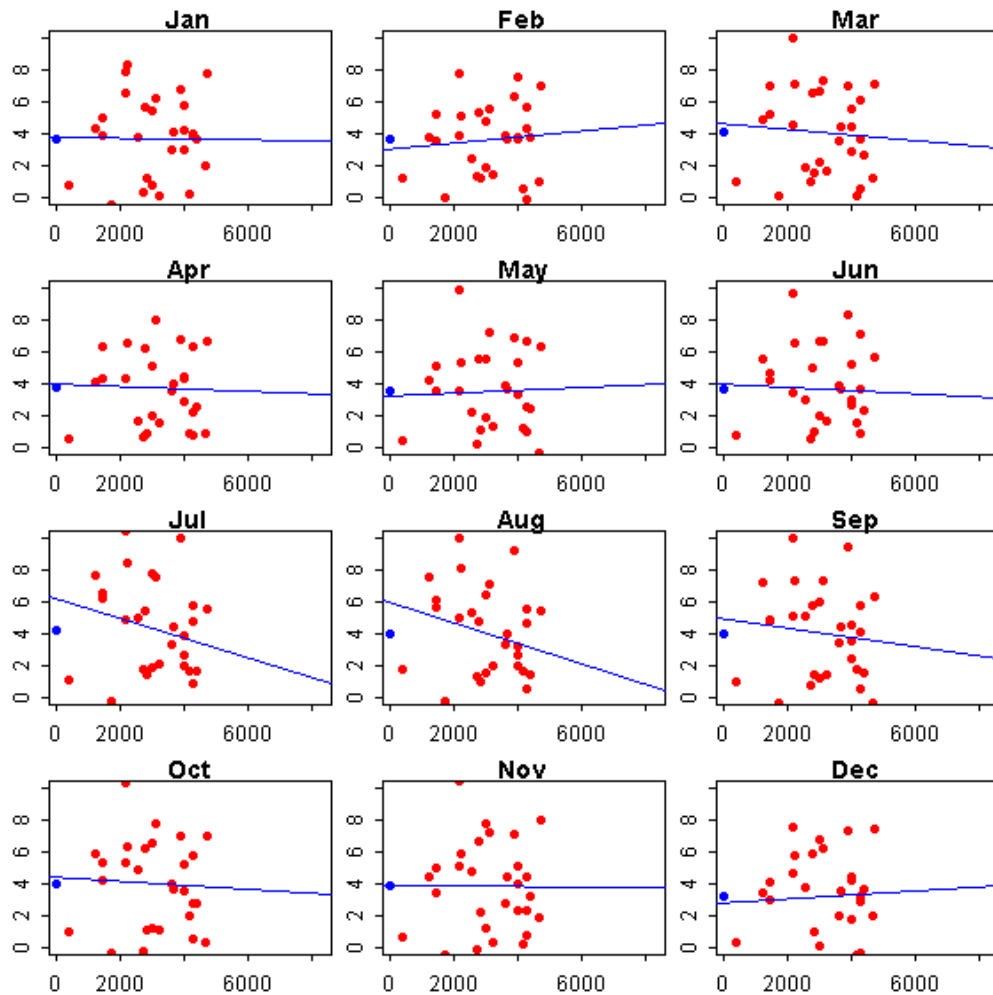


**Figure 22: Bias between observed temperatures and gridded temperatures per month (in °C, y-axis). The x-axis shows the station's elevations. Red dots represent the average bias for 29 individual stations. The blue line shows the linear regression through the red dots, the blue dots show the average bias of the 29 stations.**

We correct the ERA-INTERIM gridded temperature on a monthly scale applying the average bias correction. For each day in the original dataset running from 1 January 1981 to 31 December 2010, this is done for each grid cell:

$$T_{COR(x,y)} = T_{ERA-INT(x,y)} + a$$

where  $T_{COR}$  is the corrected temperature,  $T_{ERA-INT}$  is the original gridded temperature,  $H$  is the grid cell elevation according to the SRTM Digital Elevation Model [Farr et al., 2007], and  $a$  is the



monthly bias (blue dots in Figure 22). The corrected temperature dataset can in turn be used for the correction of the precipitation data.

### 5.1.5 Correction of precipitation data

To correct the precipitation data we use the observed glacier mass balance to derive precipitation lapse rates for each individual glacier system, as applied before in the Hunza basin and the entire upper Indus basin [Immerzeel *et al.*, 2012, 2015]. As the glaciers in the IGB cannot persist without precipitation input being higher than observed in the gridded products, we can use the glacier mass balance to derive the amount of precipitation that would be necessary to sustain the observed glacier mass balance.

Based on the conceptual model in Figure 20 we assume that precipitation increases linearly with elevation up to an elevation with maximum precipitation and decreases with the same lapse rate above that elevation:

$$P_{COR}(x, y) = P_{ERA-INT}(x, y) \cdot (1 + ((h(x, y) - h_{ref}(x, y)) \cdot \gamma \cdot 0.01))$$

for  $h < H_{MAX}$ , and:

$$P_{COR}(x, y) = P_{ERA}(x, y) \cdot \left\{ 1 + \left( \left( (h_{MAX} - h_{ref}(x, y)) + (5500 - h(x, y)) \right) \cdot \gamma \cdot 0.01 \right) \right\}$$

for  $h \geq H_{MAX}$

where  $P_{COR}$  is the corrected precipitation,  $P_{ERA}$  is the precipitation according to ERA-INTERIM,  $h_r$  is a reference elevation from which precipitation gradients occur,  $h$  is the elevation for the grid cell, and  $\gamma$  is the precipitation gradient (%  $m^{-1}$ ).

To calculate the precipitation gradients for individual glacier systems, we use geodetic mass balance data for eight sites in the HKH region [Gardelle *et al.*, 2012, 2013] (Figure 23). From these regions we select all glacier systems that have an area  $> 5 \text{ km}^2$ , which are 346 individual systems in the 8 regions in the IGB (Table 12). For each study site, [Gardelle *et al.*, 2013] used the Shuttle Radar Topographic Mission (SRTM) version 4 DEM, acquired mid-February 2000, as the reference topography. The elevation differences between the SRTM DEM and SPOT DEMs acquired between 2008 and 2011, depending on the study site, have been analysed at grid cell level and corrected for several biases except for seasonality (see [Gardelle *et al.*, 2013] for details).



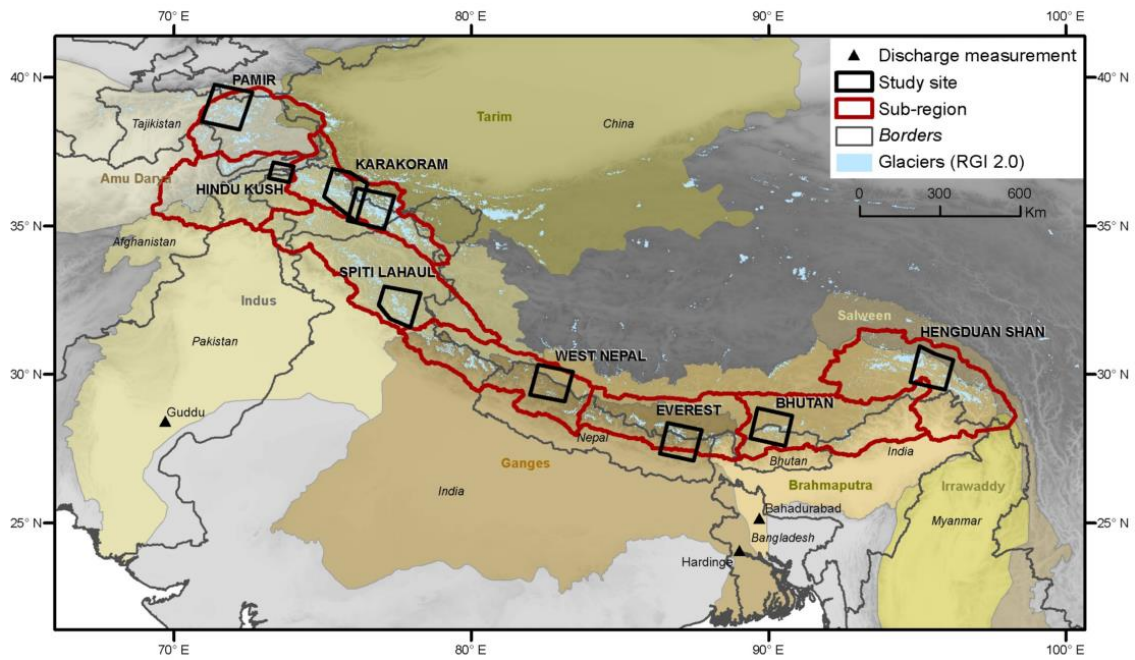


**Figure 23:** Sites in the HKH region where geodetic mass balance data has been analysed by [Gardelle et al., 2013].

**Table 12:** Properties of sites in the HKH region where geodetic mass balance data has been analysed by [Gardelle et al., 2013].

Site	Name	Date of SPOT5 DEM	No. of glaciers > 5 km <sup>2</sup>	Average MB (m we yr <sup>-1</sup> ) [Gardelle et al., 2013]	MB error (m we yr <sup>-1</sup> ) [Gardelle et al., 2013]	σ between glaciers (MB error * √n)
1	HinduKush	17-21 Oct 2008	24	-0.12	0.16	0.784
2	Karakoram West	3 Dec 2008	52	0.09	0.18	1.298
3	Karakoram East	31 Oct 2010	37	0.11	0.14	0.856
4	Spiti Lahaul	20 Oct 2011	59	-0.45	0.14	1.075
5	West Nepal	3 Jan 2011	27	-0.32	0.14	0.727
6	Everest	4 Jan 2011	43	-0.26	0.14	0.918
7	Bhutan	20 Dec 2010	45	-0.22	0.13	0.872
8	Hengduan Shan	24 Nov 2011	59	-0.33	0.14	1.075

A glacier's mass balance is determined by the amount of accumulation and the amount of ablation:

$$\Delta M = C - A$$

where C is the accumulation and A is the ablation. For each of the glacier systems the ablation can be determined using a degree day melt model forced with the corrected gridded temperature fields. This can be done quite straightforward by using the glacier outlines from a glacier inventory [Bajracharya and Shrestha, 2011] as a potential melting surface. Calculating the glacier accumulation is a bit more complex, since the accumulation area of a glacier is often not entirely included in the glacier outlines in a glacier inventory. Especially in the HKH region, the glacier accumulation consists for large part of snow fed to the glacier surface by avalanching. To include this, we assume the accumulation area of a glacier system to include



the grid cells covered by the glacier outline from the glacier inventory and in addition the adjacent grid cells that have their “drain” direction to the glacier surface and have a slope steeper than  $0.20 \text{ m m}^{-1}$ . This slope threshold is estimated from the slope distribution of the glacierised area in the UIB.

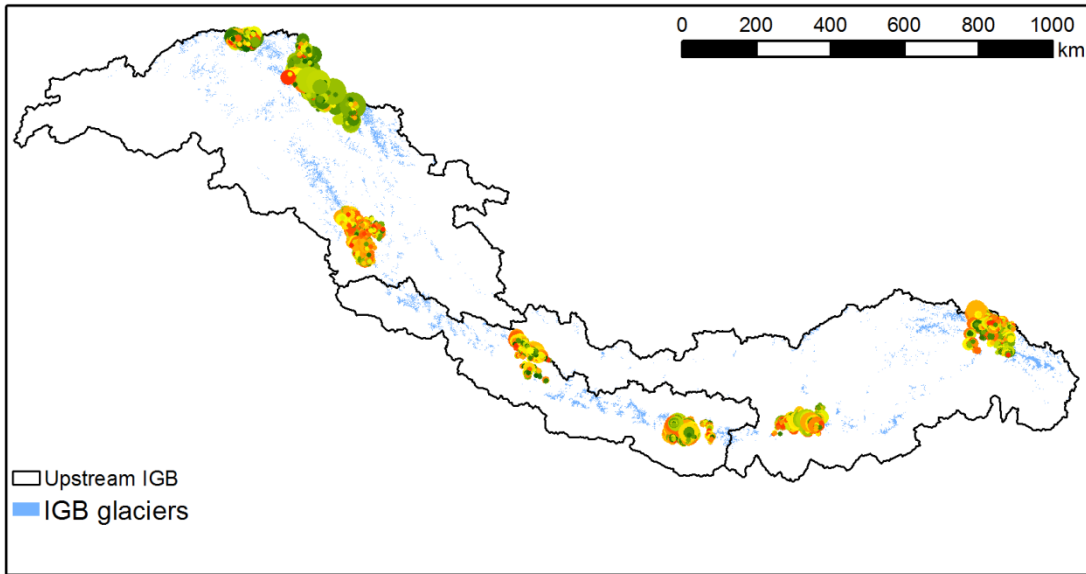


**Figure 24: Average glacier mass balance ( $\text{m we yr}^{-1}$ ) for glaciers within the geodetic mass balance analysis sites [Gardelle et al., 2013] in the upper IGB basins. Dots are scaled to glacier surface area.**

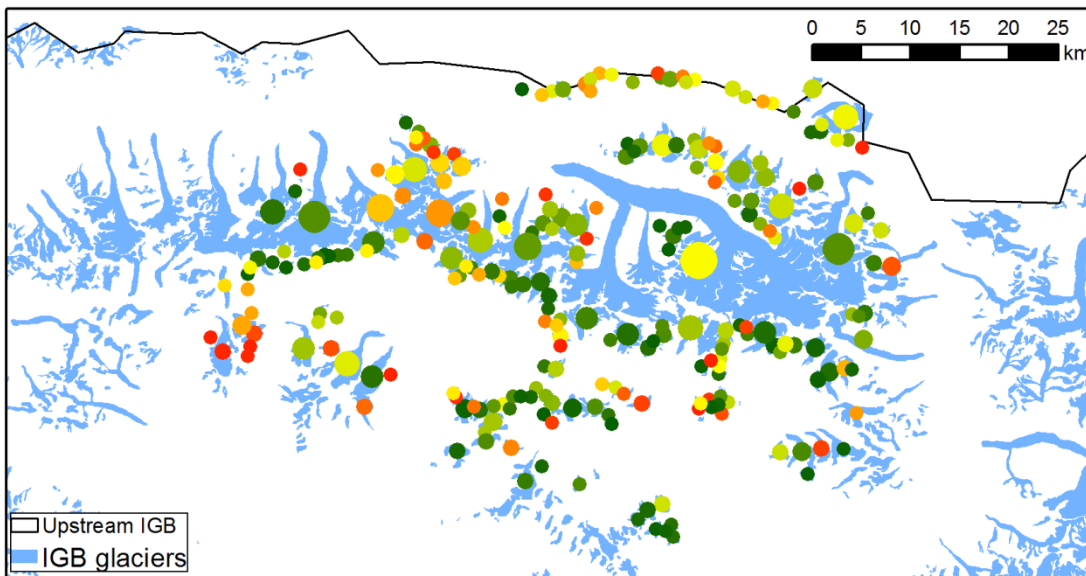


**Figure 25: Same as Figure 24, but for the Hindu Kush site.**

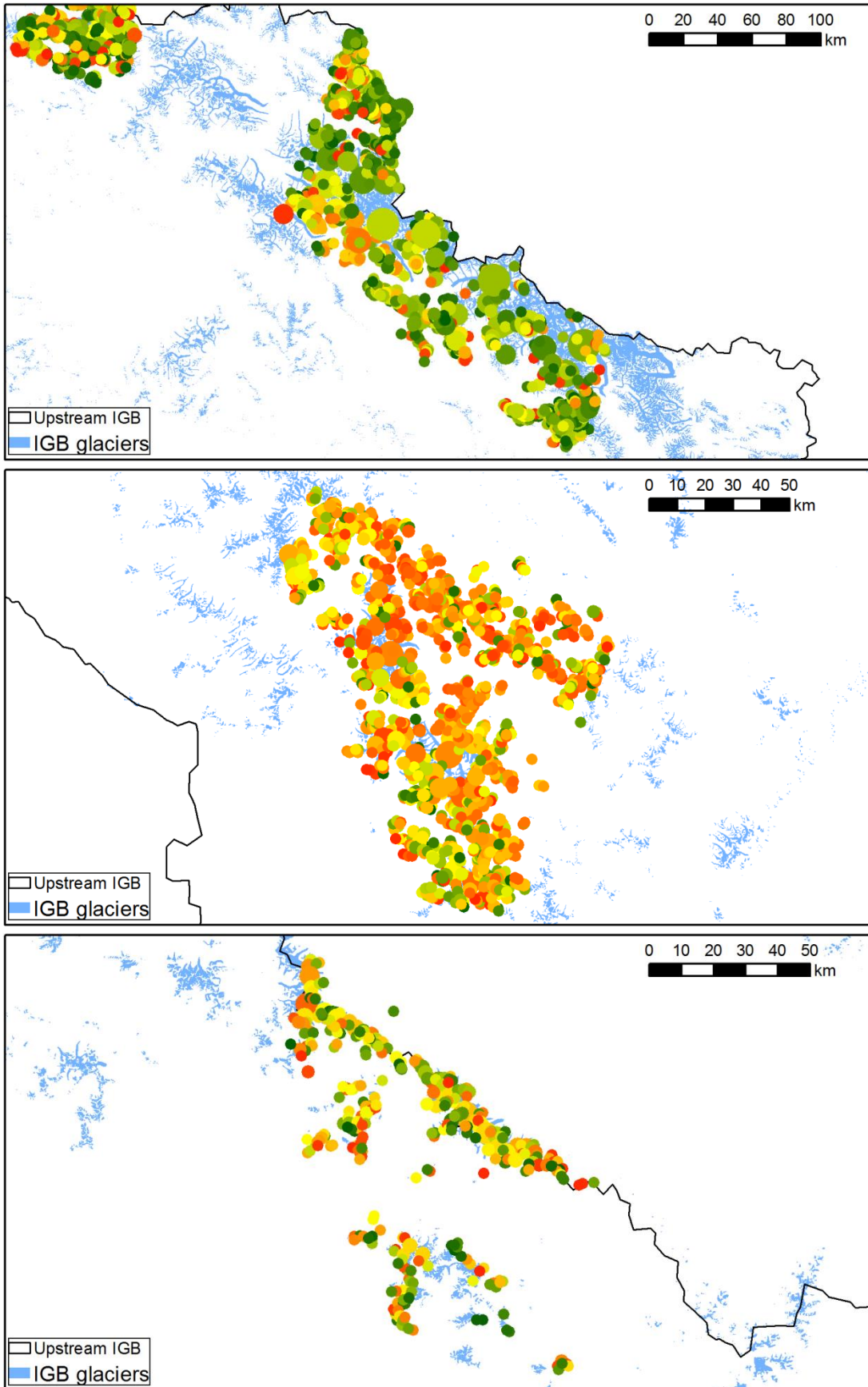


**Figure 26: Same as Figure 24, but for the Karakoram (upper panel), Spiti Lahaul (middle panel), and West-Nepal (lower panel) sites.**



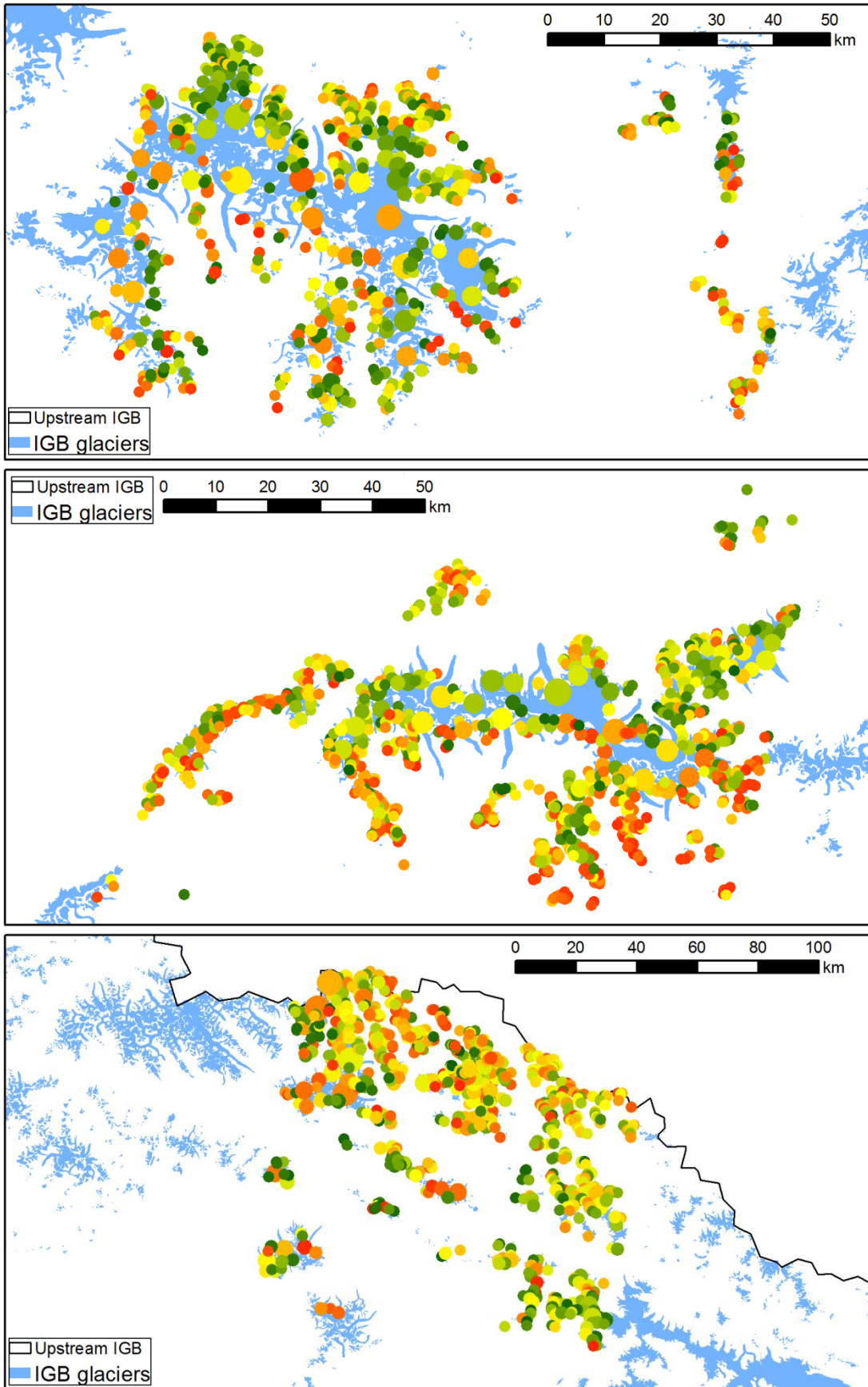


**Figure 27: Same as Figure 22, but for the Everest (upper panel), Bhutan (middle panel), and Hengduan Shan (lower panel) sites.**



Since the glacier mass balance is known and the ablation can be calculated using the melt model, we can derive for each individual glacier system which amount of precipitation would be required in the accumulation area to sustain the observed mass balance. Thus, for those glacier systems, we can derive which precipitation gradient is appropriate to correct the original precipitation field to match the amount of precipitation necessary to sustain the mass balance.

## 5.2 Statistical downscaling techniques

A number of authors have published review papers on different statistical downscaling techniques in the past 15-20 years [Wilby and Wigley, 1997; Fowler et al., 2007; Maraun et al., 2010]. In 1997, [Wilby and Wigley, 1997] categorized downscaling techniques in four categories: regression methods, weather pattern-based approaches, stochastic weather generators, and limited area modelling. Mostly downscaling approaches incorporate attributes of more than one of these techniques. [Fowler et al., 2007] also distinguish four approaches, but categorize them slightly different. They identify the 'delta change' or 'perturbation method' as the simplest statistical downscaling technique. As more sophisticated statistical downscaling methods they identify regression models, weather typing schemes and weather generators. [Maraun et al., 2010] categorize statistical downscaling methods into 'weather generators (WG)', 'perfect prognosis (PP)', and 'model output statistics (MOS)', combining the classification by [Wilby and Wigley, 1997] and a categorization based on the nature of the chosen predictors [Rummukainen, 1997]. Here we follow the categorization by [Maraun et al., 2010] to summarize different approaches to statistical downscaling, including an overview of their pro's and con's as described in the mentioned review papers and other scientific literature.

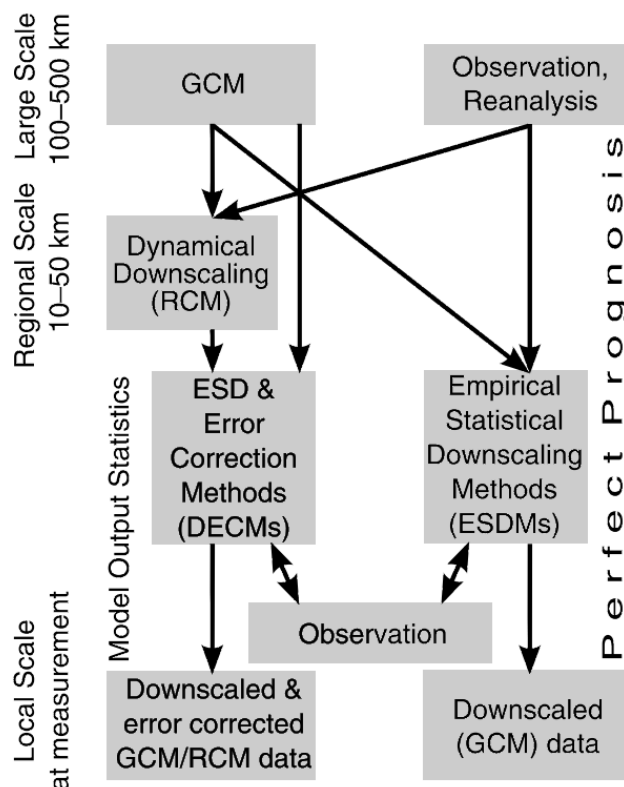


Figure 28: Scheme of different downscaling approaches (adapted from [Thiemeßl et al., 2011a]).



### 5.2.1 Perfect Prognosis Statistical Downscaling

Perfect Prognosis Statistical Downscaling approaches (or traditional empirical-statistical downscaling methods [Themeßl *et al.*, 2011b], right pathway in Figure 28) aim at establishing links between observed large-scale (synoptic scale) predictors and observed local-scale predictands. These include the classical statistical downscaling approaches including regression models and weather-pattern based approaches [Maraun *et al.*, 2010]. Regression methods were among the earliest downscaling approaches [Wilby and Wigley, 1997]. The simplest regression model is a linear regression model. In a standard linear regression model, the unexplained variability is assumed to be Gaussian distributed [Maraun *et al.*, 2010], which might be feasible to downscale annual totals of precipitation and mean air temperature, but not on shorter timescales as daily precipitation is commonly modeled using a gamma distribution. An extension of the linear model is the generalized linear model, where the predictand may follow different distributions, and the general additive model, where the linear dependency is replaced by nonparametric smooth functions. Vector generalized linear models don't solely predict the mean of a distribution, but a vector of parameters of a distribution, including for example the mean and the variance of a distribution. These models are favorable when studying the behavior of extreme events, to estimate the dependence of the variance or the extreme tail on a set of predictors [Maraun *et al.*, 2010]. In weather type-based downscaling, a set of categorical weather types are used to predict the mean of local precipitation and temperature. This approach can be considered as a special case of a linear downscaling model. Other perfect prognosis approaches are non-linear regressions like for example the use of an artificial neural network [Maraun *et al.*, 2010]. The analogue method [Zorita and Storch, 1999] is based on selecting the most similar large-scale weather situation in the past and selecting the corresponding local-scale observations. Thereby this method is limited to events that have occurred in history. The analogue method can be extended by randomly choosing the analogue from a number of most similar historical conditions [e.g. Moron *et al.*, 2008]. Physical processes on intermediate scales, like mesoscale weather patterns, are usually ignored in perfect prognosis statistical downscaling approaches.

The most basic linear regression model is the simple delta change or perturbation method [Arnell, 1999; Prudhomme *et al.*, 2002; Kay *et al.*, 2008], which downscales GCMs to local scale using change factors. Differences between a future and control GCM run are superimposed on a local-scale baseline observations dataset. Because of the simplicity of this method, a large number of GCMs can be downscaled, facilitating the possibility to use a large ensemble of possible future climates in climate change impact studies. Shortcomings of this method are the assumption that the bias between the GCM and the local-scale data remains constant in time, and only changes in the mean, minima and maxima of climatic variables are considered [Fowler *et al.*, 2007]. A climate change impact study until 2050 with application of the simple delta change method has been conducted for the IGB in ICIMOD's HICAP Programme [Lutz *et al.*, 2014a].

The Advanced Delta Change (ADC) approach [van Pelt *et al.*, 2012; Kraaijenbrink, 2013], building on previous work by [Leander and Buishand, 2007] has the advantage over the classical delta change method that not only changes in the mean are considered, but also the changes in extremes, thus making a non-linear transformation of climate signals in GCMs. Besides, changes in multi-day precipitation events are considered. The approach has been successfully applied in the Rhine basin in Europe [van Pelt *et al.*, 2012; Kraaijenbrink, 2013], and was also applied in the Upper Indus basin [Lutz *et al.*, 2014b], where some difficulties have been experienced with the downscaling of precipitation, which probably stem from the high spatial variability of meteorological variables in the high mountain environment. Additional



corrections had to be applied to correct for partly unrealistic changes in precipitation extremes. The initial nonlinear bias-correction approach developed by [Leander and Buishand, 2007] was applied to bias-correct RCM temperature and precipitation for the upper Rhone basin in Switzerland, to test its usefulness in complex, orographically influenced climate systems [Bordoy and Burlando, 2013]. They conclude that the method is able to dramatically reduce the RCM errors for both air temperature and precipitation and further conclude that the method could successfully be used for correcting future projections. However, they also observed that an undesired effect of the technique developed by [Leander and Buishand, 2007] is the generation of some extreme precipitation extreme values that considerably exceed the range of the observations.

### 5.2.2 Model Output Statistics

In Model Output Statistics (MOS) approaches (left pathway in Figure 28), the statistical relationship between predictors and predictands is established using simulated predictors and observed predictands instead of observed predictors and predictands. In most applications, the predictand is local-scale climate, and MOS combines a correction and a downscaling step. The predictors can be either simulated time series or properties of the simulated intensity distribution. The predictands can either be simulated local-scale precipitation time series or simulated local-scale intensity distributions. MOS is mostly used for RCM downscaling, while MOS application for GCM downscaling is still limited [Eden *et al.*, 2012; Eden and Widmann, 2014].

Multiple RCM post-processing methods have been developed, termed empirical-statistical downscaling and error correction methods (DECMs, left pathway in Figure 28), which are based on the MOS approach [Themeßl *et al.*, 2011b]. [Themeßl *et al.*, 2011a] tested seven DECMs for RCM-downscaling of climate for the mountainous country Austria (Figure 29), showing that point-wise methods like quantile mapping, and local intensity scaling as well as indirect spatial methods as non-linear analogue methods improve the original RCM signals.



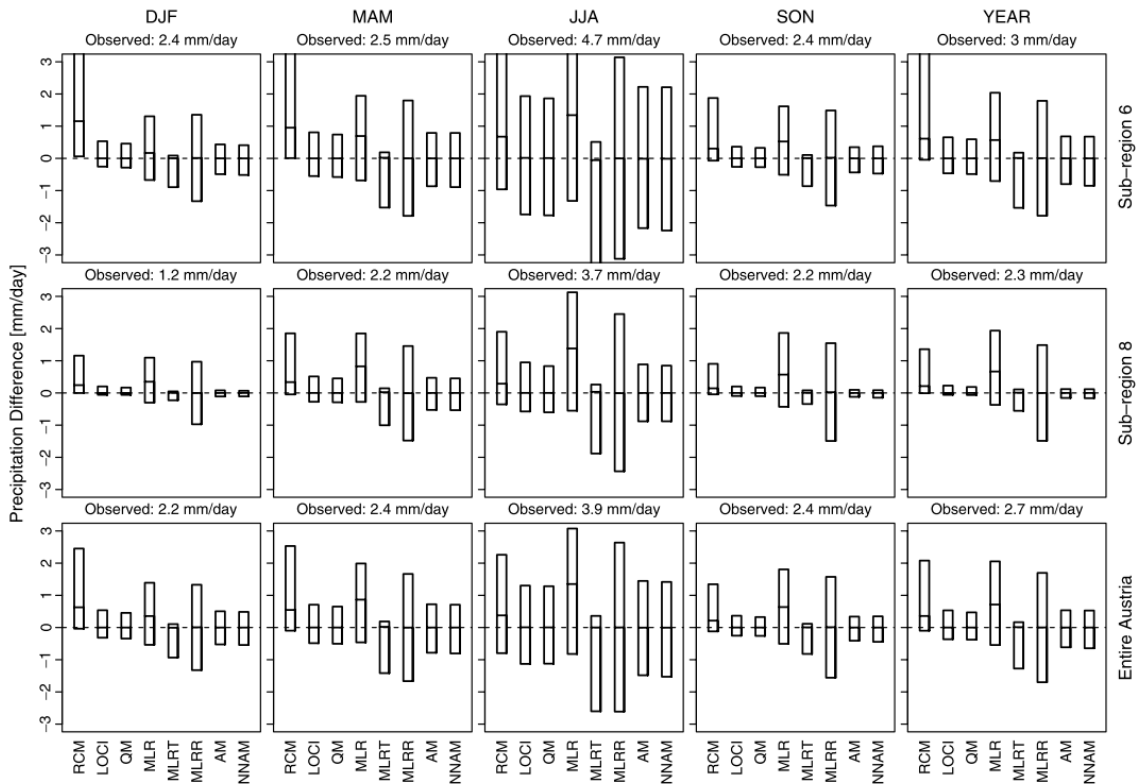


**Figure 29: Seasonal and annual errors uncorrected RCM and the seven DECMs in sub-region 6 (western Austria, high Alpine, upper panels), sub-region 8 (southeast Austria, lower Alpine, middle panels) and for entire Austria (lower panels). The boxes show the 75th percentile (upper limit), the median (line within the box) and the 25th (lower limit). The respective mean observed precipitation amount is given in the header of each panel. The statistics result from station-wise evaluation of daily precipitation data and are spatially averaged [Themeßl et al., 2011a].**

Multiple linear regression methods however, show significant shortcomings for modelling daily climate due to their linear nature. At the same time, satisfactory downscaling of precipitation is of utmost importance for mountainous areas like the upstream parts of the IGB. Local intensity scaling applies a spatially varying scaling to climate model precipitation accounting for its long-term bias at the location of the observation [e.g. Schmidli et al., 2006]. Quantile mapping [e.g. Bo et al., 2007] corrects for errors in the shape of the distribution and is therefore capable to correct errors in variability as well as the mean. According to [Themeßl et al., 2011a], in their comparison of seven DECMs over mountainous Austria, quantile mapping performed best. Adaptations in the quantile mapping method also allow for good simulation of new future extremes, which do not occur in the calibration period [Themeßl et al., 2011b]. [Immerzeel et al., 2013] successfully applied the method developed by [Themeßl et al., 2011b] to downscale GCM data at two point station locations in the HKH region.

### 5.2.3 Weather generator approaches

Weather generators are statistical models generating random sequences of weather variables, with statistical properties resembling observed weather. They are most commonly used to generate weather at point locations. The weather generator based approaches that generate spatial fields can be grouped in three categories [Ferraris et al., 2003]: Multifractal cascades, nonlinearly filtered autoregressive processes, and point processes based on the random



positioning of given number of rainfall cells. Attempts to generate continuous spatial precipitation fields have only recently been extended for downscaling [Maraun *et al.*, 2010].

[Forsythe *et al.*, 2014] combined a stochastic rainfall model and a rainfall conditioned weather generator to assess climate change signals for three point stations in a part of the Upper Indus basin. Validation to a time-series of observations at these three locations showed that the model has good skill reproducing climatological means, despite the complexity of climate in the mountainous region, at the boundary of monsoonal and westerly climate systems. Future climate was assessed using change factors derived from comparison of a future and control timeslice of an RCM.

[Bordoy and Burlando, 2014] used a stochastic downscaling approach of climate model outputs to subdaily temporal resolution for multiple point locations in the Swiss Alps. Their methodology is based on reparameterizing the Spatiotemporal Neyman-Scott Rectangular Pulses model (ST-NSRP) for future climate. Their approach showed to be robust and effective in addressing the internal variability of precipitation, as compared to other downscaling techniques which are hindered by computational and resolution problems [Bordoy and Burlando, 2014]. [Ragetti *et al.*, 2013] applied the same methodology to downscale GCM data from monthly to daily temporal resolution at three station locations in the Hunza basin in the Upper Indus basin.

### 5.3 Proposed downscaling approach for future climate

Given the mountainous nature of the upstream parts of the IGB, the downscaling methodology that has proven best performance over mountainous terrain should be used in HIAWARE. According to the comparison of downscaling methods over mountainous Austria [Themeßl *et al.*, 2011b], quantile mapping performed best in this area. Besides, the approach was applied successfully in two contrasting basins in the HKH region [Immerzeel *et al.*, 2013]. The proposed methodology builds on the work by [Themeßl *et al.*, 2011b] and [Immerzeel *et al.*, 2013], but will be extended to apply the approach to each 5x5 km pixel of the reference climate dataset for the entire IGB (including upper and lower basins). More details on the Quantile Mapping (QM) method and specific proposed application in the IGB are described in this section.

Quantile mapping is applied on a daily basis ( $t$ ) and for each grid cell ( $i$ ) separately resulting in a corrected time series  $Y^{cor}$  using a correction function (CF) as defined here [Themeßl *et al.*, 2011b]:

$$Y_{t,i}^{cor} = X_{t,i}^{raw} + CF_{t,i} \quad \text{Eq. 1}$$

$$CF_{t,i} = ecdf_{m,i}^{obs,cal^{-1}}(P_{t,i}) - ecdf_{m,i}^{mod,cal^{-1}}(P_{t,i}) \quad \text{Eq. 2}$$

$$P_{t,i} = ecdf_{m,i}^{mod,cal}(X_{t,i}^{raw}) \quad \text{Eq. 3}$$

CF represents the difference between the observed (obs) and the modeled (mod) inverse empirical cumulative density distributions ( $ecdf^{-1}$ ), for the representative day of the year (doy) in the calibration period (cal) at probability  $P$ .  $P$  is obtained by relating the raw climate model output  $X^{raw}$  to the corresponding  $ecdf$  in the calibration period. For QM calibration  $ecdfs$  are constructed for each month of the year (as in [Immerzeel *et al.*, 2013]).

Figure 30 serves as an illustrated example of the QM methodology. The upper panel shows all daily temperature observations in July during 1981-2010 and the corresponding GCM values for one grid cell.



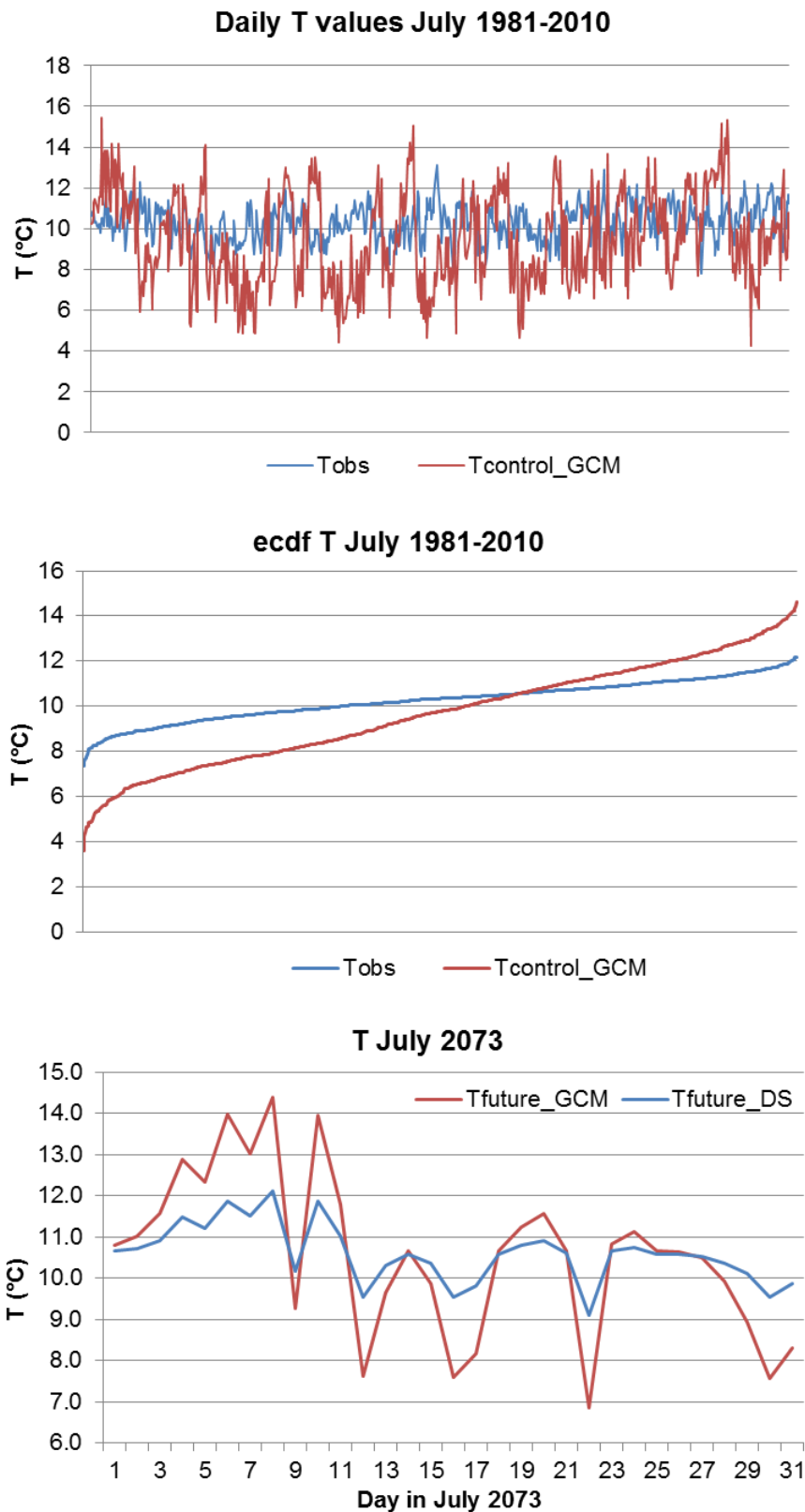


**Figure 30: Illustrative example of GCM signal downscaling by Quantile Mapping for one grid cell. Upper panel: All daily observations and GCM control run values for days in July during control period (1981-2010). Middle panel: Empirical distribution functions (ecdf) constructed for observations and GCM control run values in upper panel. Lower panel: Future daily temperature for a July in the future as from raw GCM input and corresponding downscaled values.**



For both distributions an empirical distribution function can be constructed (middle panel). With both ecdfs the correction function can be determined to correct GCM values from the future run to downscaled values (lower panel). If for example, the GCM future run projects  $T = 14\text{ °C}$  on 10 July 2073 (lower panel), then this value can be looked up in the ecdf from the GCM values in the control run (middle panel) and the corresponding value from the ecdf for observations can be determined (e.g.  $T = 12\text{ °C}$ ). Thus the downscaled value will be  $12\text{ °C}$  (lower panel). This is done for all daily values. The approach is comparative for other meteorological values, like for example precipitation (example in Figure 31).

As described in [Thiemeßl *et al.*, 2011b], the QM procedure can be extended by frequency adaptation (FA), to account for a methodological problem, occurring when the dry-day frequency in the model result is greater than in the observations, resulting in a systematic wet precipitation bias. Usually this is not the case because of the underestimate of the dry-day frequency (“drizzling effect”) in GCMs and RCMs. Problems have however been reported with the so called summer drying problems of RCMs in south-eastern Europe [e.g. Hagemann *et al.*,

2004]. With FA, only the fraction  $\Delta P_0 = \frac{(ecdf_{doy,i}^{mod,cal}(0) - ecdf_{doy,i}^{obs,cal}(0))}{ecdf_{doy,i}^{obs,cal}(0)}$  of dry-day cases with probability  $P_0$  are corrected randomly by linearly interpolating between zero precipitation and the precipitation amount of  $ecdf_{doy,i}^{mod,cal}{}^{-1}(ecdf_{doy,i}^{mod,cal}(0))$ , i.e. the first precipitation class in QM without FA). We will first test the necessity of this additional extension for the HKH region.

In addition [Thiemeßl *et al.*, 2011b] further extended the QM methodology for improved simulation of new extremes, being values of extremes outside the range of the calibration period, by including constant extrapolation of the correction value (i.e. the difference between  $ecdf^{obs,cal}$  and  $ecdf^{mod,cal}$ ) at the highest and lowest quantiles of the calibration range. Considering the example in Figure 31, a value in the future GCM run of 80 mm is outside the range of the ecdf of the GCM control run. In that case the future downscaled value would be determined as:

$$P_{Future_{DS}} = \max(P_{OBS}) \cdot \frac{P_{FUTURE_{GCM}}}{\max(P_{FUTURE_{GCM}})} = 35 \cdot \frac{80}{65} = 43\text{ mm}$$

Although the method is robust, for HIAWARE, initial testing and validation of the extended quantile mapping methodology will be done for the IGB region to ensure its applicability. The proposed methodology is as follows:

- 1) Develop a bias-corrected reference climate dataset for daily mean air temperature (Tavg), daily maximum air temperature (Tmax), daily minimum air temperature (Tmin) and daily precipitation (P). This dataset has a daily temporal resolution spanning 30 years from 1 January 1981 to 31 December 2010 and a spatial resolution of 5x5 km.
- 2) For each 5x5 km grid cell the ecdfs are determined for each of the four climatic variables (Tavg, Tmax, Tmin and P) for grid cells in the reference climate dataset for 1981-2010 and the grid cells in the GCM simulation for 1981-2010 for each month (Jan-Dec)
- 3) With the correction functions determined from the constructed future GCM data for each of the 8 GCMs, for each of the 4 meteorological parameters for each studied time slice in the future are corrected to generate downscaled hydrological model forcing.



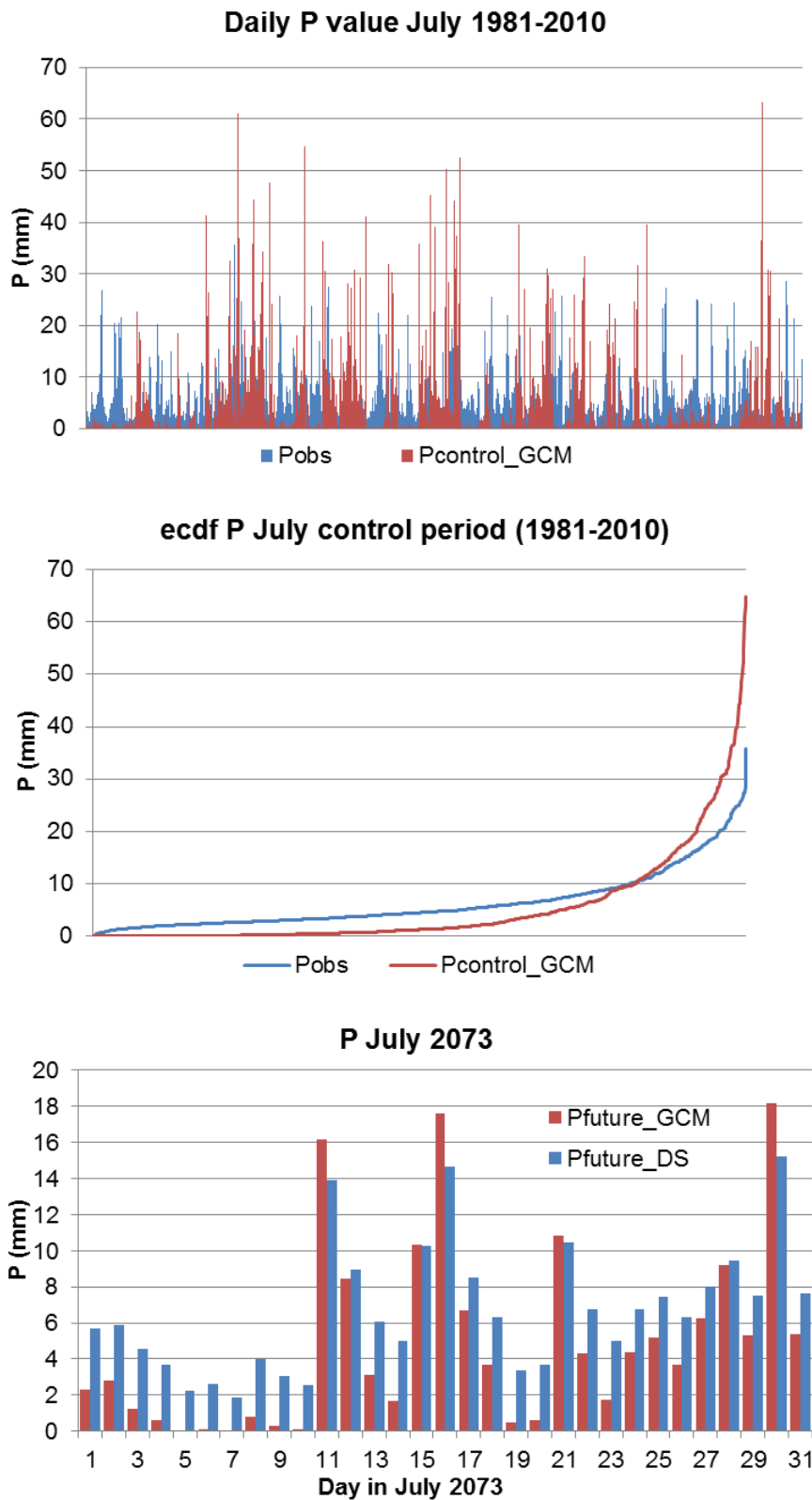


Figure 31: Illustrative example of GCM signal downscaling by Quantile Mapping for one grid cell. Upper panel: All daily observations and GCM control run values for days in July during control period (1981-2010). Middle panel: Empirical distribution functions (ecdf) constructed for observations and GCM control run values in upper panel. Lower panel: Future daily temperature for a July in the future as from raw GCM input and corresponding downscaled values.



# Appendix: Changes in indices for climatic extremes



model	$\Delta R99P$ (%)	$\Delta CDD$ (%)	$\Delta WSDI$ (%)	$\Delta CSDI$ (%)
ACCESS1-0_r1i1p1	89.1	14.9	1102.8	-91.9
bcc-csm1-1_r1i1p1	104.7	5.6	490.2	-88.8
bcc-csm1-1-m_r1i1p1	46.1	2.3	569.3	-87.4
CanESM2_r1i1p1	107.0	0.0	633.9	-96.7
CanESM2_r2i1p1	90.7	3.6	716.8	-98.1
CanESM2_r3i1p1	138.8	6.7	642.9	-95.4
CanESM2_r4i1p1	89.8	7.5	654.9	-96.3
CanESM2_r5i1p1	110.7	7.0	544.2	-97.9
CCSM4_r1i1p1	58.8	0.1	641.7	-92.8
CCSM4_r2i1p1	66.9	2.9	531.9	-84.8
CMCC-CM_r1i1p1	98.3	10.5	1162.5	-97.1
CMCC-CMS_r1i1p1	56.9	14.3	938.2	-98.4
CNRM-CM5_r1i1p1	41.9	0.7	454.2	-90.6
CSIRO-Mk3-6-0_r1i1p1	87.5	8.5	1563.9	-96.2
CSIRO-Mk3-6-0_r2i1p1	74.7	3.9	1457.2	-97.2
CSIRO-Mk3-6-0_r3i1p1	57.8	7.5	1600.8	-94.8
CSIRO-Mk3-6-0_r4i1p1	109.3	9.6	1530.3	-95.4
CSIRO-Mk3-6-0_r5i1p1	87.7	3.8	1634.4	-96.9
CSIRO-Mk3-6-0_r6i1p1	69.1	7.8	1563.8	-96.5
CSIRO-Mk3-6-0_r7i1p1	73.3	4.5	1579.8	-97.4
CSIRO-Mk3-6-0_r8i1p1	103.7	6.6	1265.4	-95.1
CSIRO-Mk3-6-0_r9i1p1	82.4	7.3	1828.7	-97.2
CSIRO-Mk3-6-0_r10i1p1	73.8	6.2	1874.9	-97.0
GISS-E2-R_r6i1p1	47.8	2.2	764.7	-81.0
GISS-E2-R_r6i1p3	84.0	8.1	763.1	-81.2
HadGEM2-CC_r1i1p1	86.5	11.8	1026.2	-96.6
HadGEM2-ES_r2i1p1	102.7	7.0	1387.6	-97.6
HadGEM2-ES_r3i1p1	89.9	12.2	1108.9	-94.5
HadGEM2-ES_r4i1p1	85.3	7.0	1006.0	-98.0
inmcm4_r1i1p1	10.5	2.9	347.5	-63.4
IPSL-CM5A-LR_r1i1p1	76.3	0.6	1039.0	-94.4
IPSL-CM5A-LR_r2i1p1	72.2	4.8	886.1	-96.3
IPSL-CM5A-LR_r3i1p1	72.9	3.8	961.0	-96.0
IPSL-CM5A-LR_r4i1p1	75.6	1.0	1003.5	-95.5
IPSL-CM5B-LR_r1i1p1	35.1	1.8	424.3	-80.7
MIROC5_r1i1p1	68.0	4.6	842.8	-98.1
MIROC5_r2i1p1	84.2	3.6	800.7	-97.1
MIROC5_r3i1p1	107.7	2.8	755.7	-98.8
MIROC-ESM_r1i1p1	52.1	4.5	820.7	-97.8
MIROC-ESM-CHEM_r1i1p1	39.5	11.0	1191.8	-92.7
MPI-ESM-LR_r1i1p1	39.6	11.5	862.5	-96.0
MPI-ESM-LR_r2i1p1	29.8	14.0	875.1	-95.8
MPI-ESM-LR_r3i1p1	43.2	13.7	961.0	-96.6
MPI-ESM-MR_r1i1p1	55.8	0.0	642.6	-90.9
MPI-ESM-MR_r2i1p1	46.6	17.6	868.8	-92.5
MPI-ESM-MR_r3i1p1	47.9	11.8	631.9	-94.2
MRI-CGCM3_r1i1p1	59.5	6.4	580.8	-94.2
NorESM1-M_r1i1p1	63.7	7.7	549.8	-89.0

Figure 32: Projected changes in climate indices between 1971-2000 and 2071-2100 for RCP4.5 multi-model ensemble.



model	$\Delta R99P$ (%)	$\Delta CDD$ (%)	$\Delta WSDI$ (%)	$\Delta CSDI$ (%)
ACCESS1-0_r1i1p1	152.2	4.9	1804.2	-97.5
bcc-csm1-1_r1i1p1	220.6	9.6	1215.6	-97.1
CanESM2_r1i1p1	219.0	17.7	1378.5	-99.6
CanESM2_r2i1p1	227.4	15.2	1623.6	-99.8
CanESM2_r3i1p1	295.5	11.7	1426.1	-100.0
CanESM2_r4i1p1	192.9	12.6	1460.6	-100.0
CanESM2_r5i1p1	261.7	10.1	1242.2	-99.8
CCSM4_r1i1p1	112.5	7.9	1451.4	-99.7
CCSM4_r2i1p1	120.9	12.5	1286.5	-97.1
CMCC-CM_r1i1p1	205.7	4.9	2225.6	-99.7
CMCC-CMS_r1i1p1	140.2	24.1	1855.1	-99.4
CNRM-CM5_r1i1p1	75.6	3.4	884.7	-99.3
CSIRO-Mk3-6-0_r1i1p1	182.0	13.8	2211.4	-99.1
CSIRO-Mk3-6-0_r2i1p1	175.5	11.6	2002.3	-99.3
CSIRO-Mk3-6-0_r3i1p1	162.9	15.8	2201.7	-98.2
CSIRO-Mk3-6-0_r4i1p1	176.9	15.5	2177.1	-99.5
CSIRO-Mk3-6-0_r5i1p1	143.2	17.6	2192.2	-99.5
CSIRO-Mk3-6-0_r6i1p1	123.1	16.4	2236.4	-99.6
CSIRO-Mk3-6-0_r7i1p1	153.9	19.3	2110.1	-98.7
CSIRO-Mk3-6-0_r8i1p1	183.3	16.1	1778.9	-98.7
CSIRO-Mk3-6-0_r9i1p1	172.2	12.4	2552.5	-98.6
CSIRO-Mk3-6-0_r10i1p1	172.1	13.4	2564.0	-98.6
HadGEM2-CC_r1i1p1	165.7	2.2	1966.3	-98.2
HadGEM2-ES_r1i1p1	185.8	1.7	2185.5	-99.4
HadGEM2-ES_r2i1p1	188.0	3.2	2427.5	-99.2
HadGEM2-ES_r3i1p1	168.4	2.4	2046.3	-99.8
HadGEM2-ES_r4i1p1	180.2	6.6	1776.3	-99.1
inmcm4_r1i1p1	30.3	5.6	905.6	-89.6
IPSL-CM5A-LR_r1i1p1	125.4	3.3	1627.4	-99.3
IPSL-CM5A-LR_r2i1p1	145.7	9.3	1346.7	-99.7
IPSL-CM5A-LR_r3i1p1	143.9	6.4	1679.0	-99.7
IPSL-CM5A-LR_r4i1p1	140.8	3.7	1651.8	-99.5
IPSL-CM5A-MR_r1i1p1	145.5	3.3	1739.9	-99.4
IPSL-CM5B-LR_r1i1p1	88.4	16.7	897.8	-97.1
MIROC5_r1i1p1	145.3	12.4	1337.8	-99.8
MIROC5_r2i1p1	207.2	8.0	1380.4	-99.8
MIROC5_r3i1p1	183.0	2.1	1429.5	-99.9
MIROC-ESM_r1i1p1	77.2	4.3	1781.7	-100.0
MIROC-ESM-CHEM_r1i1p1	71.8	27.5	2529.5	-100.0
MPI-ESM-LR_r1i1p1	103.8	24.7	2045.0	-99.6
MPI-ESM-LR_r2i1p1	74.0	22.6	1887.4	-99.5
MPI-ESM-LR_r3i1p1	87.3	24.7	2101.0	-99.8
MPI-ESM-MR_r1i1p1	90.5	4.3	1560.6	-99.8
MRI-CGCM3_r1i1p1	157.0	12.6	1452.5	-97.4
NorESM1-M_r1i1p1	151.6	0.1	1246.7	-98.8

Figure 33: Projected changes in climate indices between 1971-2000 and 2071-2100 for RCP8.5 multi-model ensemble.



## 6 References

- Andermann, C., S. Bonnet, and R. Gloaguen (2011), Evaluation of precipitation data sets along the Himalayan front, *Geochemistry, Geophys. Geosystems*, 12(7), 1–16, doi:10.1029/2011GC003513. [online] Available from: <http://doi.wiley.com/10.1029/2011GC003513> (Accessed 20 August 2013)
- Arnell, N. W. (1999), Climate change and global water resources, *Glob. Environ. Chang.*, 9, S31–S49.
- Bajracharya, S. R., and A. B. Shrestha (2011), *The Status of Glaciers in the Hindu Kush-Himalayan Region*.
- “Batura Investigations Group” (1979), The Batura Glacier in the Karakoram Mountains and its variations., *Sci. Sin.*, 22(8), 958–974.
- Boe, J., L. Terray, F. Habets, and E. Martin (2007), Statistical and dynamical downscaling of the Seine basin climate for hydro-meteorological studies Abstract., *Int. J. Climatol.*, 27, 1643–1655, doi:10.1002/joc.
- Bordoy, R., and P. Burlando (2013), Bias correction of regional climate model simulations in a region of complex orography, *J. Appl. Meteorol. Climatol.*, 52, 82–101, doi:10.1175/JAMC-D-11-0149.1.
- Bordoy, R., and P. Burlando (2014), Stochastic downscaling of precipitation to high-resolution scenarios in orographically complex regions: 1. Model evaluation, *Water Resour. Res.*, 50(November 2012), 540–561, doi:10.1002/2012WR013289.
- Christensen, J. H., and O. B. Christensen (2002), Severe summertime flooding in Europe, *Nature*, 421(February), 805–806.
- Duncan, J. M. A., and E. M. Biggs (2012), Assessing the accuracy and applied use of satellite-derived precipitation estimates over Nepal, *Appl. Geogr.*, 34, 626–638, doi:10.1016/j.apgeog.2012.04.001. [online] Available from: <http://linkinghub.elsevier.com/retrieve/pii/S0143622812000276> (Accessed 23 August 2012)
- Eden, J. M., and M. Widmann (2014), Downscaling of GCM-Simulated Precipitation Using Model Output Statistics, *J. Clim.*, 27(1), 312–324, doi:10.1175/JCLI-D-13-00063.1. [online] Available from: <http://journals.ametsoc.org/doi/abs/10.1175/JCLI-D-13-00063.1> (Accessed 24 November 2014)
- Eden, J. M., M. Widmann, D. Grawe, and S. Rast (2012), Skill, Correction, and Downscaling of GCM-Simulated Precipitation, *J. Clim.*, 25(11), 3970–3984, doi:10.1175/JCLI-D-11-00254.1. [online] Available from: <http://journals.ametsoc.org/doi/abs/10.1175/JCLI-D-11-00254.1> (Accessed 24 November 2014)
- Farr, T. G. et al. (2007), The Shuttle Radar Topography Mission, *Rev. Geophys.*, 45(RG2004).
- Ferraris, L., S. Gabellani, N. Rebora, and A. Provenzale (2003), A comparison of stochastic models for spatial rainfall downscaling, *Water Resour. Res.*, 39(12), 1–16, doi:10.1029/2003WR002504. [online] Available from: <http://doi.wiley.com/10.1029/2003WR002504> (Accessed 24 November 2014)



- Forsythe, N., H. J. Fowler, S. Blenkinsop, a. Burton, C. G. Kilsby, D. R. Archer, C. Harpham, and M. Z. Hashmi (2014), Application of a stochastic weather generator to assess climate change impacts in a semi-arid climate: The Upper Indus Basin, *J. Hydrol.*, 517, 1019–1034, doi:10.1016/j.jhydrol.2014.06.031. [online] Available from: <http://dx.doi.org/10.1016/j.jhydrol.2014.06.031>
- Fowler, H. J., S. Blenkinsop, and C. Tebaldi (2007), Linking climate change modelling to impacts studies : recent advances in downscaling techniques for hydrological modelling, *Int. J. Climatol.*, (September), 1547–1578, doi:10.1002/joc.
- Gardelle, J., E. Berthier, and Y. Arnaud (2012), Slight mass gain of Karakoram glaciers in the early twenty-first century, *Nat. Geosci.*, 5(5), 322–325, doi:10.1038/ngeo1450. [online] Available from: <http://www.nature.com/doi/10.1038/ngeo1450> (Accessed 4 March 2013)
- Gardelle, J., E. Berthier, Y. Arnaud, and a. Käab (2013), Region-wide glacier mass balances over the Pamir-Karakoram-Himalaya during 1999–2011, *Cryosph.*, 7(4), 1263–1286, doi:10.5194/tc-7-1263-2013. [online] Available from: <http://www.the-cryosphere.net/7/1263/2013/> (Accessed 18 December 2013)
- Hagemann, S., B. Machenhauer, R. Jones, O. B. Christensen, M. Deque, D. Jacob, and P. L. Vidale (2004), Evaluation of water and energy budgets in regional climate models applied over Europe, *Clim. Dyn.*, 23(5), 547–567, doi:10.1007/s00382-004-0444-7. [online] Available from: <http://link.springer.com/10.1007/s00382-004-0444-7> (Accessed 13 January 2015)
- Hay, L. E., G. J. McCabe, D. M. Wolock, and M. a. Ayers (1991), Simulation of precipitation by weather type analysis, *Water Resour. Res.*, 27(4), 493–501, doi:10.1029/90WR02650. [online] Available from: <http://doi.wiley.com/10.1029/90WR02650>
- Hewitt, K. (2005), The Karakoram Anomaly? Glacier Expansion and the “Elevation Effect,” Karakoram Himalaya, *Mt. Res. Dev.*, 25(4), 332 – 340.
- Hewitt, K. (2007a), Tributary glacier surges: an exceptional concentration at Panmah Glacier, Karakoram Himalaya, *J. Glaciol.*, 53(181), 181–188, doi:10.3189/172756507782202829. [online] Available from: <http://openurl.ingenta.com/content/xref?genre=article&issn=0022-1430&volume=53&issue=181&spage=181>
- Hewitt, K. (2007b), Tributary glacier surges: an exceptional concentration at Panmah Glacier, Karakoram Himalaya, *J. Glaciol.*, 53(181), 181–188, doi:10.3189/172756507782202829.
- Hewitt, K. (2011), Glacier Change, Concentration, and Elevation Effects in the Karakoram Himalaya, Upper Indus Basin, *Mt. Res. Dev.*, 31(3), 188–200, doi:10.1659/MRD-JOURNAL-D-11-00020.1.
- Immerzeel, W. W., F. Pellicciotti, and A. B. Shrestha (2012), Glaciers as a Proxy to Quantify the Spatial Distribution of Precipitation in the Hunza Basin, *Mt. Res. Dev.*, 32(1), 30–38, doi:10.1659/MRD-JOURNAL-D-11-00097.1.
- Immerzeel, W. W., F. Pellicciotti, and M. F. P. Bierkens (2013), Rising river flows throughout the twenty-first century in two Himalayan glacierized watersheds, *Nat. Geosci.*, 6(8), 1–4, doi:10.1038/ngeo1896. [online] Available from: <http://www.nature.com/doi/10.1038/ngeo1896> (Accessed 5 August 2013)
- Immerzeel, W. W., N. Wanders, A. F. Lutz, J. M. Shea, and M. F. P. Bierkens (2015), Reconciling high altitude precipitation with glacier mass balances and runoff, *Hydrol. Earth Syst. Sci. Discuss.*, 12, 4755–4784, doi:10.5194/hessd-12-4755-2015.



- Karl, T. R., W.-C. Wang, M. E. Schlesinger, R. W. Knight, and D. Porthman (1990), A method of Relating General Circulation Model Simulated Climate to the Observed Local Climate. Part I: Seasonal Statistics, *J. Clim. Clim.*, 3, 1053–1079.
- Kay, A. L., H. N. Davies, V. A. Bell, and R. G. Jones (2008), Comparison of uncertainty sources for climate change impacts: flood frequency in England, *Clim. Change*, 92, 41–63, doi:10.1007/s10584-008-9471-4. [online] Available from: <http://www.springerlink.com/index/10.1007/s10584-008-9471-4> (Accessed 13 July 2012)
- Kjellström, E., F. Boberg, M. Castro, J. H. Christensen, G. Nikulin, and E. Sánchez (2010), Daily and monthly temperature and precipitation statistics as performance indicators for regional climate models, *Clim. Res.*, 44, 135–150, doi:10.3354/cr00932.
- Kraaijenbrink, P. (2013), *Advanced Delta Change method*, De Bilt, The Netherlands.
- Leander, R., and T. A. Buishand (2007), Resampling of regional climate model output for the simulation of extreme river flows, *J. Hydrol.*, 332, 487–496, doi:10.1016/j.jhydrol.2006.08.006.
- Lutz, A. F., W. W. Immerzeel, A. B. Shrestha, and M. F. P. Bierkens (2014a), Consistent increase in High Asia's runoff due to increasing glacier melt and precipitation, *Nat. Clim. Chang.*, 4, 587–592, doi:10.1038/NCLIMATE2237.
- Lutz, A. F., W. W. Immerzeel, and P. D. A. Kraaijenbrink (2014b), *Gridded Meteorological Datasets and Hydrological Modelling in the Upper Indus Basin. FutureWater Report 130*, Wageningen, The Netherlands.
- Maraun, D. et al. (2010), Precipitation downscaling under climate change: recent developments to bridge the gap between dynamical models and the end user, *Rev. Geophys.*, 48(RG3003), 1–34.
- Maussion, F., D. Scherer, T. Mölg, E. Collier, J. Curio, and R. Finkelburg (2014), Precipitation Seasonality and Variability over the Tibetan Plateau as Resolved by the High Asia Reanalysis, *J. Clim.*, 27(5), 1910–1927, doi:10.1175/JCLI-D-13-00282.1. [online] Available from: <http://journals.ametsoc.org/doi/abs/10.1175/JCLI-D-13-00282.1> (Accessed 7 November 2014)
- Moron, V., A. W. Robertson, M. N. Ward, and O. Ndiaye (2008), Weather Types and Rainfall over Senegal. Part II: Downscaling of GCM Simulations, *J. Clim.*, 21(2), 288–307, doi:10.1175/2007JCLI1624.1. [online] Available from: <http://journals.ametsoc.org/doi/abs/10.1175/2007JCLI1624.1> (Accessed 10 November 2014)
- Moss, R. H. et al. (2010), The next generation of scenarios for climate change research and assessment., *Nature*, 463(7282), 747–56, doi:10.1038/nature08823. [online] Available from: <http://www.ncbi.nlm.nih.gov/pubmed/20148028> (Accessed 9 July 2014)
- Palazzi, E., J. Von Hardenberg, and A. Provenzale (2013), Precipitation in the Hindu-Kush Karakoram Himalaya : Observations and future scenarios, *J. Geophys. Res. Atmos.*, 118, 85–100, doi:10.1029/2012JD018697.
- Van Pelt, S. C., J. J. Beersma, T. a. Buishand, B. J. J. M. van den Hurk, and P. Kabat (2012), Future changes in extreme precipitation in the Rhine basin based on global and regional climate model simulations, *Hydrol. Earth Syst. Sci.*, 16(12), 4517–4530, doi:10.5194/hess-16-4517-2012.
- Perkins, S. E., A. J. Pitman, N. J. Holbrook, and J. McAneney (2007), Evaluation of the AR4 climate models' simulated daily maximum temperature, minimum temperature, and



- precipitation over Australia using probability density functions, *J. Clim.*, *20*, 4356–4376, doi:10.1175/JCLI4253.1.
- Prudhomme, C., N. Reynard, and S. Crooks (2002), Downscaling of global climate models for flood frequency analysis: where are we now?, *Hydrol. Process.*, *16*(6), 1137–1150, doi:10.1002/hyp.1054. [online] Available from: <http://doi.wiley.com/10.1002/hyp.1054> (Accessed 3 November 2014)
- Ragetti, S., F. Pellicciotti, R. Bordoy, and W. W. Immerzeel (2013), Sources of uncertainty in modeling the glacio-hydrological response of a Karakoram watershed to climate change, *Water Resour. Res.*, *49*, 1–19, doi:10.1002/wrcr.20450. [online] Available from: <http://doi.wiley.com/10.1002/wrcr.20450> (Accessed 24 September 2013)
- Rummukainen, M. (1997), *Methods for statistical downscaling of GCM simulations*.
- Sanchez, E., R. Romera, M. A. Gaertner, C. Gallardo, and M. Castro (2009), A weighting proposal for an ensemble of regional climate models over Europe driven by 1961–2000 ERA40 based on monthly precipitation probability density functions, *Atmos. Sci. Lett.*, *10*, 249–254, doi:10.1002/asl.
- Schmidli, J., C. Frei, and P. L. Vidale (2006), Downscaling from GCM precipitation: a benchmark for dynamical and statistical downscaling methods, *Int. J. Climatol.*, *26*(5), 679–689, doi:10.1002/joc.1287. [online] Available from: <http://doi.wiley.com/10.1002/joc.1287> (Accessed 24 November 2014)
- Sillmann, J., V. V. Kharin, X. Zhang, F. W. Zwiers, and D. Bronaugh (2013a), Climate extremes indices in the CMIP5 multimodel ensemble: Part 1. Model evaluation in the present climate, *J. Geophys. Res. Atmos.*, *118*(4), 1716–1733, doi:10.1002/jgrd.50203. [online] Available from: <http://doi.wiley.com/10.1002/jgrd.50203> (Accessed 10 July 2014)
- Sillmann, J., V. V. Kharin, F. W. Zwiers, X. Zhang, and D. Bronaugh (2013b), Climate extremes indices in the CMIP5 multimodel ensemble: Part 2. Future climate projections, *J. Geophys. Res. Atmos.*, *118*(6), 2473–2493, doi:10.1002/jgrd.50188. [online] Available from: <http://doi.wiley.com/10.1002/jgrd.50188> (Accessed 16 July 2014)
- Taylor, K. E., R. J. Stouffer, and G. A. Meehl (2012), An Overview of CMIP5 and the Experiment Design, *Bull. Am. Meteorol. Soc.*, *93*(4), 485–498, doi:10.1175/BAMS-D-11-00094.1.
- Thiemeßl, M. J., A. Gobiet, and A. Leuprecht (2011a), Empirical-statistical downscaling and error correction of daily precipitation from regional climate models, *Int. J. Climatol.*, *31*(10), 1530–1544, doi:10.1002/joc.2168. [online] Available from: <http://doi.wiley.com/10.1002/joc.2168> (Accessed 6 November 2014)
- Thiemeßl, M. J., A. Gobiet, and G. Heinrich (2011b), Empirical-statistical downscaling and error correction of regional climate models and its impact on the climate change signal, *Clim. Change*, *112*(2), 449–468, doi:10.1007/s10584-011-0224-4.
- Turner, A. G., and H. Annamalai (2012), Climate change and the South Asian summer monsoon, *Nat. Clim. Chang.*, *2*, 587–595, doi:10.1038/nclimate1495.
- Van Vuuren, D. P., E. Stehfest, M. G. J. den Elzen, J. van Vliet, and M. Isaac (2010), Exploring IMAGE model scenarios that keep greenhouse gas radiative forcing below 3W/m<sup>2</sup> in 2100, *Energy Econ.*, *32*(5), 1105–1120, doi:10.1016/j.eneco.2010.03.001. [online] Available from: <http://linkinghub.elsevier.com/retrieve/pii/S014098831000037X> (Accessed 16 October 2014)
- Van Vuuren, D. P. et al. (2011), RCP2.6: exploring the possibility to keep global mean temperature increase below 2°C, *Clim. Change*, *109*, 95–116, doi:10.1007/s10584-011-



0152-3. [online] Available from: <http://link.springer.com/10.1007/s10584-011-0152-3>  
(Accessed 26 September 2014)

Vuuren van, D. P. et al. (2011), The representative concentration pathways: an overview, *Clim. Change*, 109(1-2), 5–31, doi:10.1007/s10584-011-0148-z. [online] Available from: <http://link.springer.com/10.1007/s10584-011-0148-z> (Accessed 22 May 2013)

Weedon, G. P., G. Balsamo, N. Bellouin, S. Gomes, M. J. Best, and P. Viterbo (2014), The WFDEI meteorological forcing data set: WATCH Forcing Data methodology applied to ERA-Interim reanalysis data Graham, *Water Resour. Res.*, 7505–7514, doi:10.1002/2014WR015638.

Wilby, R. L., and T. M. L. Wigley (1997), Downscaling general circulation model output: a review of methods and limitations, *Prog. Phys. Geogr.*, 21(4), 530–548, doi:10.1177/030913339702100403. [online] Available from: <http://ppg.sagepub.com/cgi/doi/10.1177/030913339702100403> (Accessed 19 August 2013)

Winiger, M., M. Gumpert, and H. Yamout (2005), Karakorum-Hindukush-western Himalaya: assessing high-altitude water resources, *Hydrol. Process.*, 19(12), 2329–2338, doi:10.1002/hyp.5887.

Zorita, E., and H. Storch (1999), The Analog Method as a Simple Statistical Downscaling Technique : Comparison with More Complicated Methods, *J. Clim.*, 12, 2474–2489.

